Cell Reports

Resource

Deciphering the Dynamic Transcriptional and Post-transcriptional Networks of Macrophages in the Healthy Heart and after Myocardial Injury

Graphical Abstract

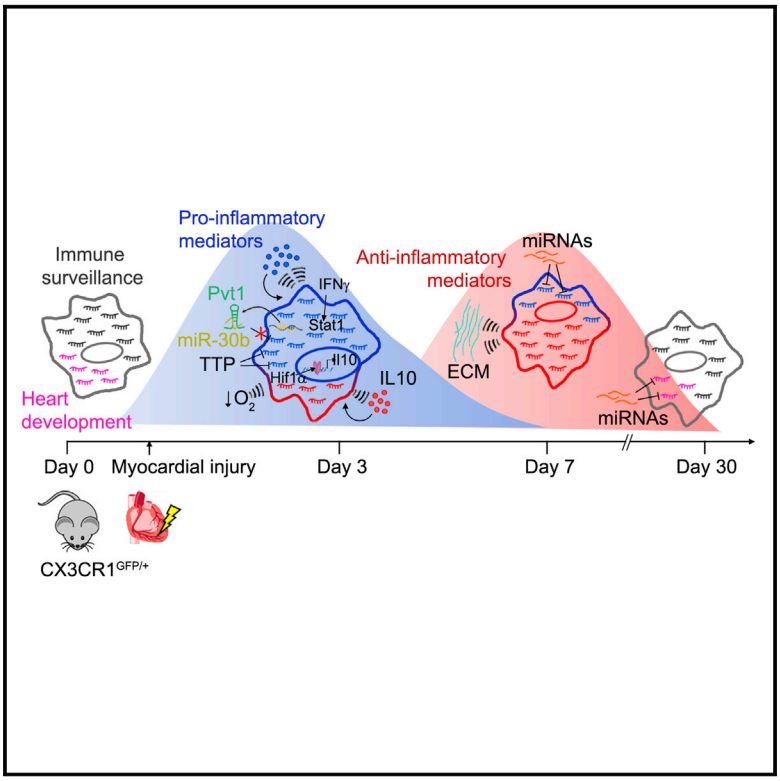

Authors

Wencke Walter, Laura Alonso-Herranz, Verdiana Trappetti, ..., Alicia G. Arroyo, Fátima Sánchez-Cabo, Mercedes Ricote

Correspondence

fscabo@cnic.es (F.S.-C.), mricote@cnic.es (M.R.)

In Brief

Walter et al. generate a whole transcriptome dataset (mRNA, miRNA, and lincRNA) of macrophages in the healthy heart and after myocardial injury. This study reveals that post-injury macrophages simultaneously activate pro- and anti-inflammatory programs. Furthermore, they identified transcriptional and post-transcriptional mechanisms regulating myocardial injury-induced inflammation.

Highlights

- A comprehensive resource of the mouse cardiac macrophage transcriptional profile
- Macrophages involved in cardiac repair do not align to canonical M1/M2 programs
- Endogenous and exogenous feedback loops regulate phenotype transition after injury
- Identified markers might serve as targets for specific therapeutic intervention

Data and Software Availability

GSE97147

Walter et al., 2018, Cell Reports *23*, 622–636
April 10, 2018
https://doi.org/10.1016/j.celrep.2018.03.029

CellPress

OPEN ACCESS
CellPress

Cell Reports
Resource

Deciphering the Dynamic Transcriptional and Post-transcriptional Networks of Macrophages in the Healthy Heart and after Myocardial Injury

Wencke Walter,[1,5] Laura Alonso-Herranz,[1,5] Verdiana Trappetti,[1] Isaac Crespo,[2] Mark Ibberson,[2] Marta Cedenilla,[1] Anna Karaszewska,[1] Vanessa Núñez,[1] Ioannis Xenarios,[2] Alicia G. Arroyo,[3] Fátima Sánchez-Cabo,[4,*] and Mercedes Ricote[1,6,*]

[1]Myocardial Pathophysiology Area, Centro Nacional de Investigaciones Cardiovasculares Carlos III (CNIC), 28029 Madrid, Spain
[2]Vital-IT, SIB Swiss Institute of Bioinformatics, University of Lausanne, 1015 Lausanne, Switzerland
[3]Vascular Pathophysiology Area, Centro Nacional de Investigaciones Cardiovasculares Carlos III (CNIC), 28029 Madrid, Spain
[4]Bioinformatics Unit, Centro Nacional de Investigaciones Cardiovasculares Carlos III (CNIC), 28029 Madrid, Spain
[5]These authors contributed equally to this work
[6]Lead Contact
*Correspondence: fscabo@cnic.es (F.S.-C.), mricote@cnic.es (M.R.)
https://doi.org/10.1016/j.celrep.2018.03.029

SUMMARY

Macrophage plasticity has been studied *in vitro*, but transcriptional regulation upon injury is poorly understood. We generated a valuable dataset that captures transcriptional changes in the healthy heart and after myocardial injury, revealing a dynamic transcriptional landscape of macrophage activation. Partial deconvolution suggested that post-injury macrophages exhibit overlapping activation of pro-inflammatory and anti-inflammatory programs rather than aligning to canonical M1/M2 programs. Furthermore, simulated dynamics and experimental validation of a regulatory core of the underlying gene-regulatory network revealed a negative-feedback loop that limits initial inflammation via hypoxia-mediated upregulation of *Il10*. Our results also highlight the prominence of post-transcriptional regulation (miRNAs, mRNA decay, and lincRNAs) in attenuating the myocardial injury-induced inflammatory response. We also identified a cardiac-macrophage-specific gene signature (e.g., *Egfr* and *Lifr*) and time-specific markers for macrophage populations (e.g., *Lyve1*, *Cd40*, and *Mrc1*). Altogether, these data provide a core resource for deciphering the transcriptional network in cardiac macrophages *in vivo*.

INTRODUCTION

Macrophages (Mφs) are multifunctional cells of the innate immune system that reside in all tissues, contributing to their development, homeostasis, and protection against pathogens and injury (Davies et al., 2013; Gautier et al., 2012). Mφs are morphologically and functionally heterogeneous, a reflection of the diversity of tissue environments in which they reside. They are very plastic cells that continuously shift their functional phenotype to new states in response to microenvironmental changes (Sica et al., 2015). In addition to maintaining tissue homeostasis and responding to invading pathogens, Mφs contribute to numerous pathological processes, making them potentially attractive targets for therapeutic intervention (Harel-Adar et al., 2011; Sica et al., 2015). Such interventions will, however, require detailed understanding of Mφ molecular biology in different tissues and disease contexts.

Extensive research into Mφ activation using *in vitro* models has led to Mφs being classified according to a bipolar model. M1 or classically activated Mφs are elicited by pro-inflammatory signals such as lipopolysaccharide (LPS) and interferon-γ (IFN-γ), whereas anti-inflammatory signals such as interleukin-4 (IL-4) and IL-13, lead to M2 or alternatively activated Mφs (Sica et al., 2015). Growing evidence indicates that this *in vitro* model is an oversimplification and has limited ability to explain the broad variety of phenotypes encountered *in vivo* (Varga et al., 2016). Recent studies have aimed to characterize the molecular signature of Mφs in resting tissues (Gautier et al., 2012; Gosselin et al., 2014; Lavin et al., 2014). However, very little is known about Mφ transcriptional and post-transcriptional activation during inflammation and the subsequent healing response *in vivo*.

Following myocardial injury, inflammatory monocytes are recruited from the bone marrow and spleen and enter the damaged tissue to give rise to Mφs (Heidt et al., 2014; Hilgendorf et al., 2014; Nahrendorf et al., 2007; Swirski et al., 2009). These recruited Mφs clear necrotic cellular debris and damaged extracellular matrix (ECM) from the tissue and attract other immune cells through the secretion of pro-inflammatory cytokines and chemokines such as tumor necrosis factor α (TNF-α), IL-1β, and IL-6. However, due to their high plasticity, Mφs not only are able to initiate the inflammatory response but also play a critical role in resolving inflammation, and at later post-injury stages have the capacity to dampen inflammation and promote ECM reconstruction, cell proliferation, and angiogenesis (Hilgendorf et al., 2014; Nahrendorf et al., 2007). These Mφs are characterized by the secretion of anti-inflammatory and profibrotic factors such as IL-10 and transforming growth factor β (TGF-β), which promote tissue repair. These opposing functions are most likely carried out by distinct Mφ populations. However, the exact

identities of these Mφs remain undefined, and it is not well understood how this transition from pro-inflammatory to anti-inflammatory activities is orchestrated *in vivo*.

Recent advances in omics technologies have opened up the possibility to address these questions and to elucidate transcriptional programs and the spatiotemporal properties of the underlying multifaceted regulatory networks. Recent studies addressed the transcriptional regulation in cardiac Mφs (Epelman et al., 2014; Pinto et al., 2012; Yan et al., 2017), but while these studies were focused on the healthy heart, our work fills the void of an integrative study that deciphers the different levels of transcriptional regulation in cardiac homeostasis and after injury. Here, we used a systems biology approach to gain understanding of Mφs in the healthy and post-injury heart by combining mathematical modeling and computational biology with experimental data. Our study focused not only on the response to injury of protein-coding RNAs (mRNAs) but also on microRNA (miRNA) and long intergenic noncoding RNA (lincRNA) profiles, in order to better define the different modes of Mφ activation in cardiac repair. Furthermore, we collected published data on gene-regulatory interactions to create a prior knowledge network (PKN) and used Boolean logic to identify stable states within it based on our gene expression data (Albert, 2007; Garg et al., 2009; Rodriguez et al., 2015).

Hypotheses derived from the inferred model were validated by *in vitro* experiments and revealed a negative-feedback loop that potentially contributes to the observed switch between the pro- and anti-inflammatory responses post-injury. This dataset provides a valuable resource for extending knowledge of Mφ biology and expanding the growing collection of molecular signatures of immune-related cells in different contexts and tissues.

RESULTS

$CX_3CR1^{GFP/+}$ Mice as a Model for Analyzing Mφs in the Healthy and Injured Heart

Cryoinjury was induced in $CX_3CR1^{GFP/+}$ knockin mice (Jung et al., 2000), in which Mφs can be tracked (Heidt et al., 2014; Hulsmans et al., 2017; Pinto et al., 2012; Varga et al., 2016). An extensive inflammatory response was observed in the early post-injury stage, followed by the deposition of a fibrotic scar at later post-injury stages (Figure S1A), and resulting in cardiac dysfunction (Figures S1B and S1C). To study Mφ responses, we isolated GFP^+ cells at steady state and different post-injury stages, applying a widely used fluorescence-activated cell sorting (FACS) gating strategy (Heidt et al., 2014; Pinto et al., 2012; Varga et al., 2016) (Figures S2A and S2B). The diversity of Mφ subsets in the myocardium has been reported (Epelman et al., 2014). However, our goal was to gain an unbiased picture of the transcriptional regulation and function of the total Mφ population in cardiac healing. Cell quantification (Figure S2C) clearly shows the predominance of the $Ly6C^{low}/CX_3CR1^{high}$ population at 0 days, contrasting an increase in the $Ly6C^{high}/CX_3CR1^{low}$ population at 3 days post-injury, corresponding to the recruitment of monocyte-derived Mφs (Heidt et al., 2014). At 7 and 30 days, the most abundant population is $Ly6C^{low}/CX_3CR1^{high}$ cells. Hence, $Ly6C^{low}/CX_3CR1^{high}$ cells were taken to assess the characteristics of cardiac-resident Mφs (CRMs) (day 0) and in the reparative phase (7 and 30 days post-injury), whereas $Ly6C^{high}/CX_3CR1^{low}$ cells were selected to characterize Mφs in the inflammatory phase (3 days post-injury) (Varga et al., 2016). Our cell populations were distinguished from monocytes by the expression of the core Mφ signature marker CD64 (Gautier et al., 2012) and the classical Mφ markers F4/80 and CD68 at all stages by flow cytometry (Figure S2D) and by confocal fluorescence microscopy (Figure S2E). To elucidate the dynamic transcriptional landscape of *in vivo* Mφs, we purified Mφ populations from single-cell suspensions of digested hearts at different post-injury stages by FACS (Figures S2A and S2B). Global gene expression profiles of purified cells were obtained by RNA-sequencing (RNA-seq) and miRNA profiling.

Cardiac Mφs Display a Unique and Tissue-Specific Gene Signature

Mφs reside in nearly all tissues of the body and have been shown to differ in their ontological origin, epigenetic imprinting, and gene expression (Gautier et al., 2012; Gosselin et al., 2014; Lavin et al., 2014). We aimed to extend these findings to CRMs by comparing them with two published databases (GEO: GSE15907 and GSE63340) of tissue-resident Mφs (TRMs) (Gautier et al., 2012; Lavin et al., 2014). Principal-component analysis (PCA) and pairwise correlation analysis of the samples supported previous findings indicating that TRMs can be distinguished by their gene expression (Figures 1A and S3A). To explore this heterogeneity in more detail, we used k-means clustering (k = 15; Figure S3B; Table S1) to identify sets of tissue-specific co-expressed genes. The clustering revealed a previously undescribed set of cardiac-Mφ-specific genes (Figure S3B, cluster XII). Although we applied batch correction (Supplemental Experimental Procedures), comparisons among different datasets could be affected by limitations. We therefore qPCR-validated the cardiac-specific expression of some of the identified genes (*Lifr*, *Egfr*, *Myh6*, *Il1rl1*, *Osmr*, and *Steap4*) (Figures 1B, S3C, S3D, and S4A). Expression of leukemia inhibitory factor receptor (LIFR) and epidermal growth factor receptor (EGFR) on the CRM surface was confirmed by flow cytometry (Figure 1B).

Mφs from the Healthy and Injured Hearts Have Different Transcriptional Signatures

PCA of the global transcriptional profiles of all samples revealed clear separation between the different post-injury stages (Figure S4B). Unsupervised k-means clustering (k = 6; Figure 1C) of 4,988 differentially expressed genes (DEGs) (Figure S4C; Tables S2 and S3) revealed three clusters with time-point-specific gene signatures. Cluster I included genes specifically expressed in CRMs, such as cardiomyocyte structural genes (e.g., *Myl2*, *Myh6*, *Tnnt2*), and was enriched in heart development and myofibril assembly related genes (Figures 1C and 1D; Table S2). This cluster was also enriched for cell adhesion genes (e. g. *Lyve-1*, *Cd36*), possibly indicating close interactions between Mφs and other cardiac cells in the healthy heart. Cluster II contained genes specifically expressed in Mφs isolated at day 3. These genes were enriched for immune response (e.g., *Cd274*, *Stat1*, *Ccl2*), programmed cell death (e.g., *Tnfrsf21*, *Xaf1*, *Itpr1*), apoptotic signaling (e.g., *Cd40*, *Casp8*, *Spp1*), and regulation of reactive oxygen species (ROS) metabolic

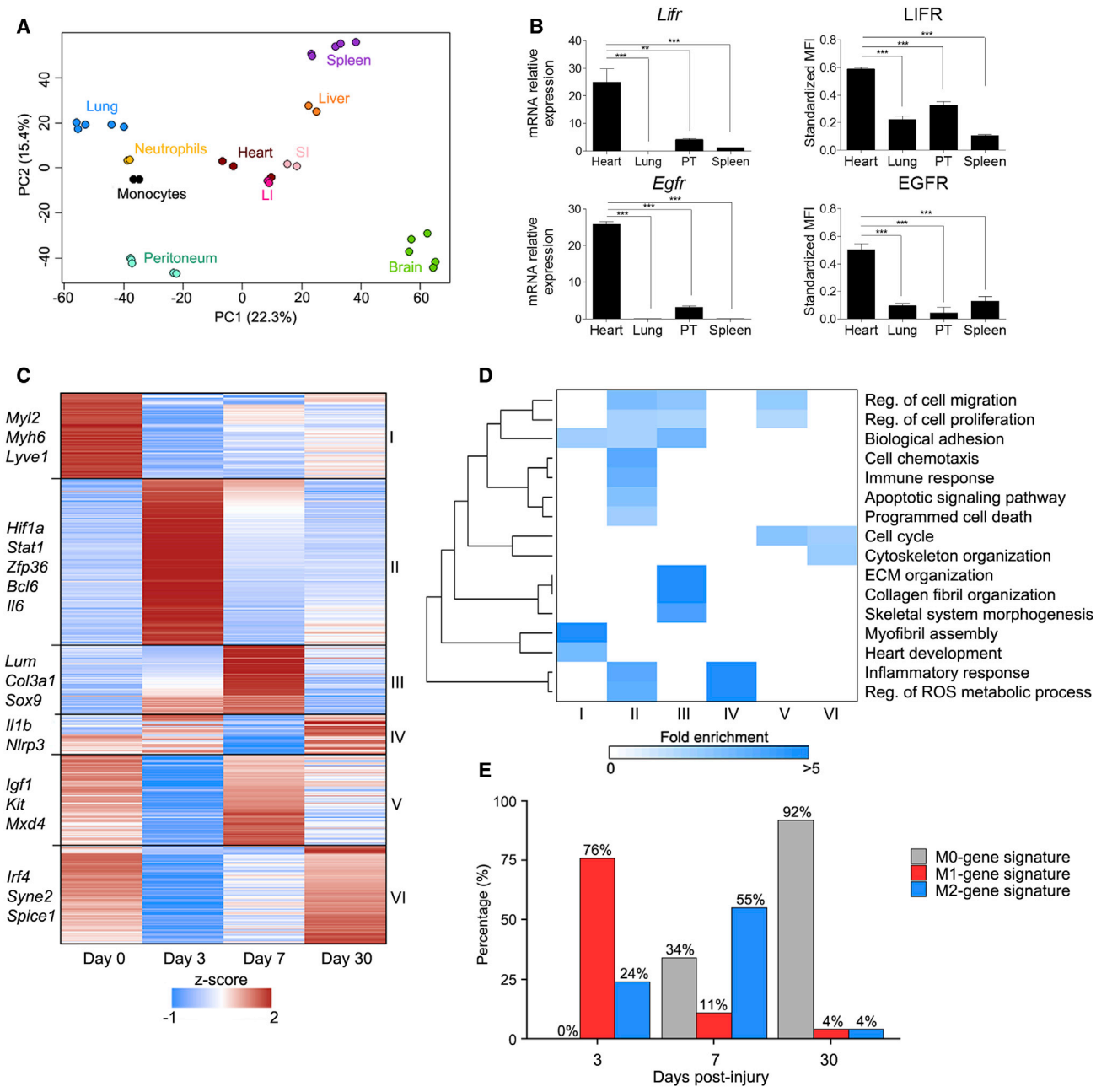

Figure 1. Transcriptional and Functional Characterization of Mφs in the Healthy Heart and after Injury

(A) PCA of tissue-resident Mφs, comparing the transcriptional profile of heart Mφs with published expression sets of other tissue-resident Mφs (GSE15907, GSE63340).

(B) qPCR and flow cytometry validation of surface markers specific for CRMs. Data are shown as mean or median ± SEM of three independent experiments; **p < 0.01, ***p < 0.001 (one-way ANOVA followed by Tukey test).

(C) K-means clustering (k = 6) of the 4,988 DEGs in at least one time point compared with control.

(D) HC of significantly enriched PANTHER biological processes (Benjamini-Hochberg adjusted p [B-H adj-p] < 0.01; fold enrichment > 2).

(E) CellMix-estimated frequency of M0, M1, and M2 gene signatures (using published expression database GSE53321 of *in vitro* BMDM treated with various stimuli) in *in vivo* samples at different post-injury stages.

See also Figures S1–S4 and Tables S1 and S2.

processes (e.g., *Ptegs2*, *Xdh*, *Acod1*) (Figures 1C and 1D; Table S2). The upregulation at 3 days post-injury of *Hif1a* and its target genes *Vegfa*, *Glut1*, and *Pgk1* may indicate a hypoxic environment (Figure 1C; Table S2). Interestingly, 20% of these genes (e.g., *Stat1*, *Zfp36*, *Il6*) are potential targets of IFN-γ (Rusinova et al., 2013). Genes specifically expressed in Mφs

isolated at 7 days post-injury (cluster III) were associated with ECM and collagen fibril organization (e.g., *Lum*, *Col3a1*), indicating an active role in tissue remodeling (Figures 1C and 1D; Table S2). The enrichment of cell proliferation regulators in the same cluster (e.g., *Sox9*, *Sox4*, Figures 1C and 1D; Table S2) is in accordance with previous findings in Mφs isolated after skeletal muscle injury (Varga et al., 2016). Cluster IV contained relevant immune related genes characterized by down-regulation of their expression at day 7 (e.g., *Il1b*, *Cxcl2*, *Nlrp3*; Figures 1C and 1D; Table S2).

K-means clustering also revealed a shared transcriptional signature between CRMs and Mφs isolated at day 7 (cluster V), and CRMs and Mφs at day 30 (cluster VI). Enrichment of cluster V for genes involved in cell cycle and cell proliferation processes (e.g., *Igf1*, *Kit*, *Mxd4*; Figures 1C and 1D; Table S2) would confirm the self-renewal potential of CRMs (Epelman et al., 2014) and the proliferative capacity of Mφs involved in tissue repair (Hilgendorf et al., 2014; Varga et al., 2016). On the other hand, genes with elevated expression on day 0 and day 30 (cluster VI) were mainly involved in cell-cycle processes (e.g., *Spice1*, *Nuf2*) and cytoskeleton organization (e.g., *Syne2*), indicating restoration of homeostasis at 30 days post-injury (Figures 1C and 1D; Table S2).

The Transcriptional Profiles of Post-injury Mφs Are a Mix of the Gene Signatures of Described *In Vitro* Phenotypes

Examination of genes in cluster II (3 days post-injury Mφs) revealed simultaneous expression of M1 markers (e.g., *Ccr2*, *Stat1*, *Il6*, *Cxcl10*) and M2 markers (e.g., *Arg1*, *Msr1*, *Stat3*, *Tgfb1*) (Table S2). Similar mixed expression of M1 genes (e.g., *Ccr7*, *Ccl8*) and M2 genes (e.g., *Trem2*, *Clec2i*) occurred in cluster III (7 days post-injury Mφs) (Table S2). These results suggest that *in vivo* Mφs are transcriptional hybrids of the phenotypes described *in vitro*.

In order to test this hypothesis computationally, partial deconvolution was used to evaluate the M1 and M2 phenotype contribution to the *in vivo* samples. Partial deconvolution has become a useful tool for estimating cell-type frequencies within heterogeneous gene expression samples (Shen-Orr et al., 2010). The gene expression profile of CRMs (M0), BMDMs activated with LPS plus IFN-γ (M1), and BMDMs activated with IL-4 plus IL-13 (M2), taken from published *in vitro* database GSE53321 (Li et al., 2015), were used as reference profiles to estimate the contributions of the M0, M1, and M2 gene signatures to the post-injury Mφ population *in vivo* using partial deconvolution (Shen-Orr et al., 2010) (see Experimental Procedures for further detail). The estimated frequencies of the M0, M1, and M2 gene signature within post-injury Mφs are shown in Figure 1E. The transcriptional profile of Mφs isolated at 3 days post-injury was driven by M1 associated genes (76% M1) but already included anti-inflammatory genes (24% M2). The profile retained no gene expression pattern reminiscent of CRMs (0%). Gene expression at 7 days post-injury was mainly characterized by M2-associated genes (55%) but retained transcriptional traces of a M1 gene signature (11%). This result suggests a transition from pro-inflammatory to anti-inflammatory further continuing to resting Mφ, as indicated by the contribution of the M0 profile. The latest post-injury stage was completely dominated by the M0 gene signature (92%). Altogether, these results reveal that post-injury cardiac Mφs cannot be defined as canonical M1 or M2 Mφs. Instead, we report dynamic transcriptional changes in Mφs during tissue repair.

The Signaling Receptome and Secretome Program of Cardiac Mφs Depends on the Activation State

The secretome and receptome were identified within each cluster (Table S3; Supplemental Experimental Procedures). Interestingly, the highest relative abundance of genes encoding for the secretome occurred on day 7 and was nearly double the relative abundance of the receptome (cluster III, Figure 2A), indicating an increased heterotypic paracrine signaling potential. Functional analysis associated the identified secretome with regulation of angiogenesis and blood vessel development, and ECM and collagen fibril organization-related processes (Figure S5A), suggesting a key role of Mφs in cell signaling through the secretion of angiogenic factors (e.g., *Hgf*, *Figf*, *Srpx2*) and ECM components (e.g., *Col3a1*, *Lox*, *Postn*) during the reparative post-injury phase (Figure 2B; Table S3). The secretome and receptome components expressed by Mφs during the inflammatory phase (cluster II, day 3) were consistently associated with the immune response (e.g., *Cd40*, *Cd44*, *Cxcl10*), leukocyte migration and leukocyte chemotaxis (e.g., *Ccl7*, *Ccl12*, *Cxcl3*), and blood vessel development (e.g., *Angpt2*, *Mmp19*, *Vegfa*) (Figures 2B, 2D, and S5A; Table S3). In addition, we found numerous potential secretome-receptome interactions (e.g., *Ccl12-Cxcr4*, *Cxcl3-Cxcr2*, *Ccl7-Ccr5*) (Figure 2C; Table S3), suggesting that Mφs sustain the inflammatory response through homotypic paracrine signaling. At 3 days post-injury, Mφs expressed *Ccl2* (Figure 2B), suggesting recent infiltration by circulating monocytes and promotion of further monocyte recruitment to the inflammation site (Sica et al., 2015). CRMs (cluster I) expressed secretome components associated with angiogenesis regulation (e.g., *Mmp9*, *Cx3cl1*) (Figure 2B), and this finding was supported by the receptome components identified (e.g., *Lyve-1*, *Esam*) (Figures 2B and 2D; Table S3). In addition, leukocyte chemotaxis and immune response processes were enriched (Figure S5A), supporting the role of CRMs in immune surveillance. The secretome of CRMs and 7 days post-injury Mφs (cluster V) was associated with biological adhesion (e.g., *Nid1*, *Lama5*, *Lamb2*) and ECM and collagen-related processes (e.g., *Mmp11*, *Col4a1*, *Dpt*) (Figure S5A; Table S3), indicating a fundamental role of these Mφs in the maintenance of tissue integrity. Secretome and receptome components with elevated expression on days 0 and 30 included anti-inflammatory genes (e.g., *Ccl17*, *Ccl22*, *Mrc1*, *Cd86*), supporting the immune quiescent phenotype of CRMs (Figures 2B and 2D; Table S3). The low number of potential homotypic signaling pairs in the healthy heart and at 30 days post-injury (Figure 2C; Table S3) suggests that the receptome has a primarily immune surveillance function. Additionally, specific surface markers (*Lyve1*, *Cd36*, *Cd40*, *Cd274*, *Cd86*, and *Mrc1*) were validated by qPCR and flow cytometry for the different Mφ populations at each stage (Figure 2D). Cells were isolated using the gating strategy shown in Figures S5B and S5C.

The Complex Regulatory Network of *In Vivo* Cardiac Mφs

Sequence-based motif enrichment analysis (Supplemental Experimental Procedures) of genes in each cluster (Figure 3A)

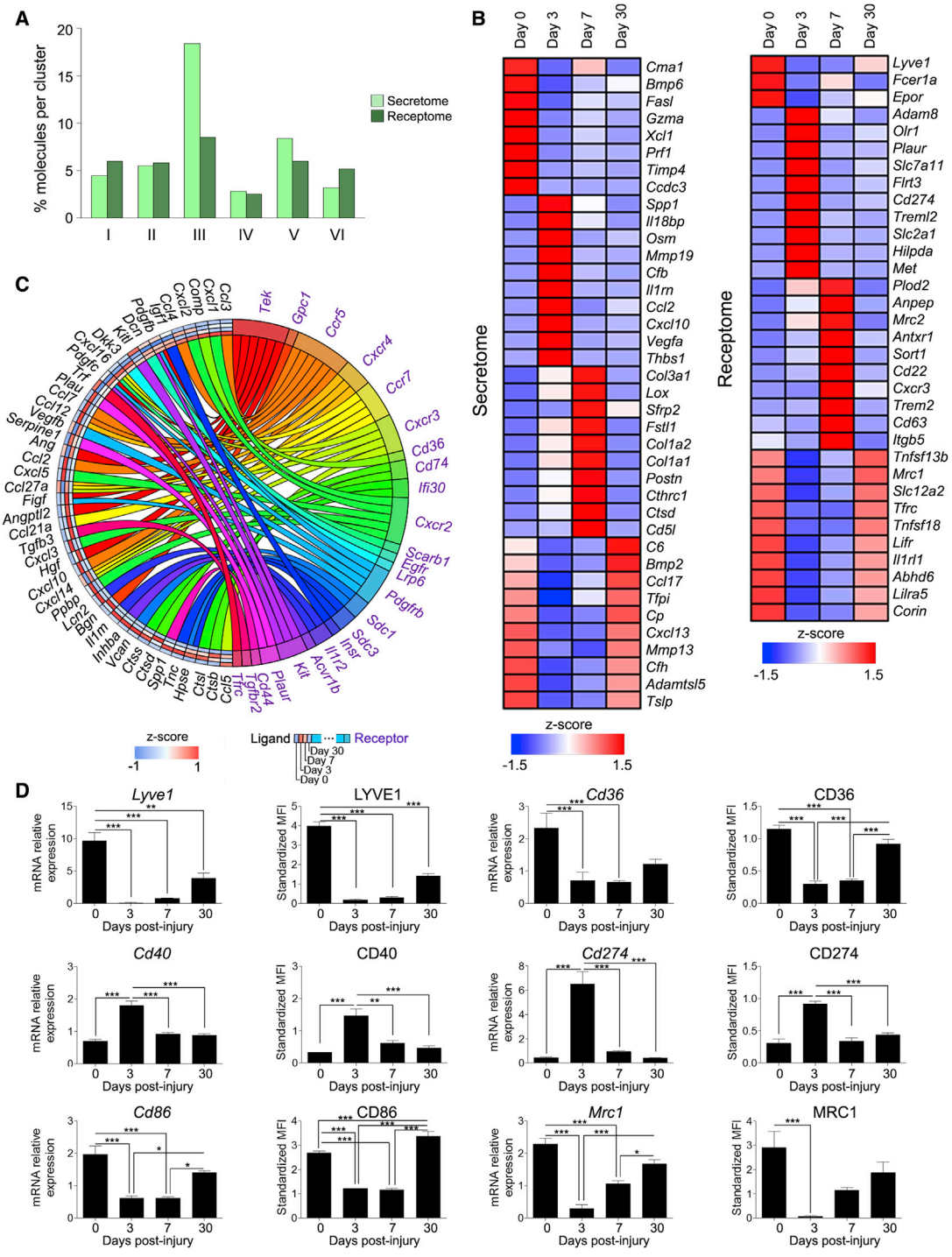

Figure 2. Transcriptional Profile of the Cardiac Mφ Secretome and Receptome

(A) Relative abundance of secretome and receptome components per cluster.

(B) Secretome and receptome heatmap for clusters I, II, III, and VI. Molecules with logFC > 1 in all relevant contrasts were kept, ranked by significance, and a maximum of 10 per cluster selected.

(C) Chord diagram of secretome (black)-receptome (purple) interactions. Squares alongside secretome gene symbols indicate the z scores 0, 3, 7, and 30 days post-injury.

(D) qPCR and flow cytometry validation of selected surface markers. Data are shown as mean or median ± SEM of three independent experiments; *p < 0.05, **p < 0.01, ***p < 0.001 (one-way ANOVA followed by Tukey test).

See also Figure S5 and Table S3.

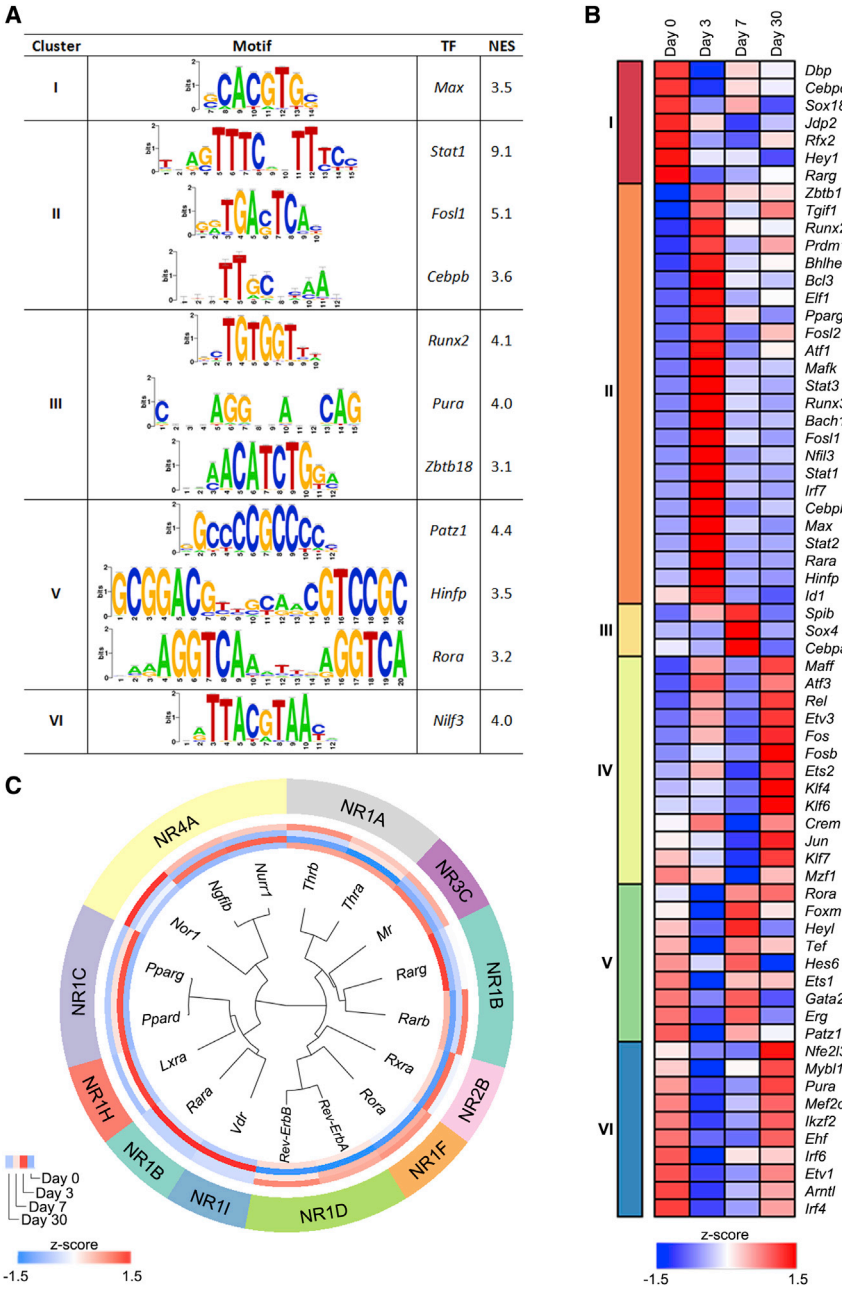

Figure 3. Sequence-Based Motif Enrichment Analysis of Genes in Each Cluster Identified DE TFs with Heterogeneous Expression Profiles

(A) Motifs enriched in the promoter region of clustered genes (Figure 1C). For each cluster, the motifs are shown with the highest normalized enrichment score up to a maximum of 3. The selected motifs are linked to their corresponding TF. Only TFs that changed across conditions were considered.

(B) Expression z scores of each DE TF linked to the enriched motifs. Profiles were grouped according to cluster.

(C) GOCluster of DE nuclear receptors clustered by family. The inner ring represents the z-score profile (see legend).

identified 66 differentially expressed (DE) transcription factors (TFs) with heterogeneous expression profiles (Figure 3B), revealing a complex regulatory program of Mφs upon injury. Within the six clusters, 17 nuclear receptors could be identified (Figure 3C). Interestingly, CRMs showed elevated retinoid signaling (*Rarg*, *Rarb*, *Rxra*), a crucial pathway in cardiac development (Rhinn and Dollé, 2012), which is consistent with the biological process enrichment of cluster I (Figure 1D). Moreover, at day 3 we found an upregulation of *Pparg* and *Ppard* (Figure 3C), which regulate M2-like gene expression patterns (Glass and Saijo, 2010). We also found upregulation of the positive immune regulators *Vdr*, *Ngfib*, and *Nurr1* (Glass and Saijo, 2010), consistent with the pro-inflammatory function of these Mφs (Figure 3C).

Following the workflow depicted in Figure S6A, a PKN (Rodriguez et al., 2015) was built based on the 251 DEGs included in the top ten most enriched pathways (Figure S6B; Experimental Procedures). IL-6 and type II IFN signaling pathways were enriched 3 days post-injury. Focal adhesion PI3K-Akt-mTOR and TGF-β signaling pathways were enriched at 7 and 30 days post-injury, respectively. The PKN was further extended with experimentally validated interactions and the subnetworks with significant temporal changes in expression were identified (Ideker et al., 2002).

Network structure analysis of the most significant subnetwork revealed a strongly connected component (SCC) (Albert, 2007) consisting of 21 genes (Figure 4A). Within the SCC, each gene is connected to every other through a directed path, and changes in the state of one gene can thus affect the other genes in the SCC (Albert, 2007). We therefore analyzed the core network stability. A Boolean dynamical model with an asynchronous updating scheme was used to compute network stable states (Garg et al., 2009). Despite training the network with a time series of four time points, computation of SCC stability revealed only three stable states. This result is consistent with the finding of only three time point-specific clusters and the high similarity of the global transcriptional profiles on days 0 and 30 post-injury (Figure 1C). We identified one stable state with all nodes "off," indicating a non-activated or deactivated state that may be associated with CRMs and Mφs isolated on post-injury day 30 (Figure S6C). Another stable state was found for the onset of *Prdm1*, *Bcl6*, *Stat3*, and *Eomes* (Figure S6C). *Prdm1* is a known transcriptional repressor that in mouse Mφs

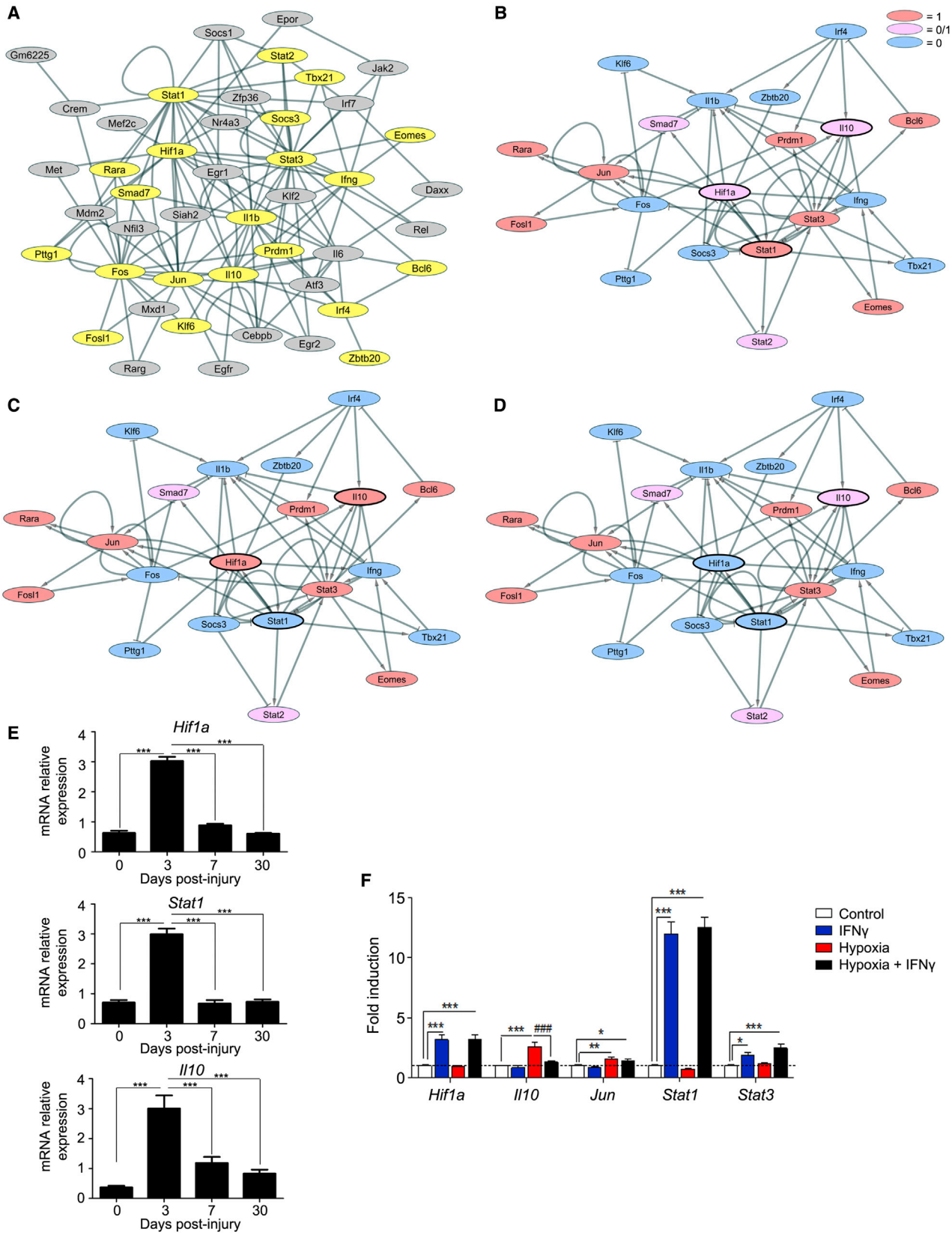

(legend on next page)

becomes activated in response to cellular stress (Tooze et al., 2006). *Bcl6* negatively regulates Mφ proliferation by inhibiting *Il6* autocrine signaling (Yu et al., 2005), and *Eomes* has been associated with cell differentiation (Pearce et al., 2003). The transcription of all three genes is regulated by *Stat3*, which can trigger a pro-inflammatory or anti-inflammatory program depending on the strength and duration of its activation (Braun et al., 2013). The onset of these factors indicates a more repressive, anti-inflammatory state and may be associated with Mφs on post-injury day 7. The third stable state was mainly characterized by oscillation in the activation of *Hif1a*, *Stat1*, and *Il10* (Figures 4B–4D). Whereas *Hif1a* and *Stat1* are associated with a pro-inflammatory program (Sica et al., 2015; Takeda et al., 2010), *Il10* is a powerful anti-inflammatory mediator that plays a fundamental role in the transition from the inflammatory to the resolution phase of the immune response (Lambert et al., 2008). The upregulated genes suggest an activation of both the pro-inflammatory and the anti-inflammatory programs, linking this stable state to Mφs isolated on day 3 post-injury, a conclusion supported by qPCR expression profiles (Figure 4E).

The oscillatory pattern of this stable state suggests that the regulation of *Il10* is tightly intertwined with the expression of *Hif1a* and *Stat1*, whereas a positive regulatory effect of *Hif1a* on *Il10* expression seems to be diminished by the presence of *Stat1*, as indicated by the changes in the node states (Figures 4B–4D). *Hif1a* is the main mediator of the hypoxic response, and hypoxic conditions can positively alter *Il10* expression (Cai et al., 2013), whereas IFN-γ has a negative effect on *Il10* expression through suppression of CREB and AP-1 activity (Hu et al., 2006). Based on this result, we hypothesized that hypoxia, but not IFN-γ, leads to the induction of *Il10*.

To test this hypothesis *in vitro*, we conducted qPCR to assess the expression of a panel of cycle attractor genes (Figures 4F, S6D, and S6E). In agreement with a previous report (Takeda et al., 2010), we observed strong upregulation of *Hif1a* by IFN-γ and combined treatment with IFN-γ and hypoxia, whereas hypoxic conditions alone did not upregulate *Hif1a* mRNA (Figure 4F). However, *Hif1a* expression is regulated at the post-mRNA level (Kaelin and Ratcliffe, 2008), and upregulation of *Hif1a* target genes confirmed its activation by hypoxia (Figure S6D). We also detected increased *Il10* expression in hypoxic conditions but not in response to IFN-γ or combined treatment with IFN-γ and hypoxia, confirming our hypothesis. Combined treatment with IFN-γ and hypoxia also induced the expression of *c-Jun*, whereas expression of *Stat1* and *Stat3* was exclusively altered by IFN-γ and did not change in hypoxic conditions (Figure 4F).

The Cardiac Mφ miRnome in the Healthy and Injured Heart

Following the workflow shown in Figure S7A, we studied the miRnome of cardiac Mφs in the healthy heart and after injury. PCA of the global transcriptional profiles revealed well-separated miRNA expression signatures at the different post-injury stages (Figure S7B). Comparison of each post-injury stage with the control sample and all other stages identified 255 non-redundant miRNAs DE in at least one comparison (Figure S7C; Table S4). Hierarchical clustering (HC) of the DE miRNAs revealed heterogeneous expression profiles, indicating activity of the same miRNA during different phases of cardiac repair (Figure S7D).

Next, we constructed a global miRNA-mRNA interaction network of all DEGs and associated DE miRNAs (Figure 5A, Table S5; Supplemental Experimental Procedures) and identified three main subnetworks (S1, S2, S3; Table S5). Post-transcriptional regulation of genes in subnetwork S1 is controlled by miRNAs (e.g., mmu-miR-328, mmu-miR-125a, and mmu-miR-99b; Figure S7E; Table S5) that downregulated genes in CRMs and in Mφs at 7 and 30 days post-injury. S1 genes were associated with the inflammatory response and chemokine production (Figure 5B), suggesting miRNA regulation of inflammatory processes and resolution of inflammation at day 7, further supported by the downregulation of inflammatory-related genes in cluster IV (Figures 1C and 1D; Table S2) at day 7, and restoration of homeostasis at 30 days post-injury. The second subnetwork (S2; Table S5) is controlled by miRNAs upregulated at day 3 and downregulated in CRMs. Expression of these miRNAs at day 3 (e.g., mmu-miR-504 and mmu-miR-181d; Figure S7E; Table S5) downregulates cell-cycle genes (Figure 5B). In addition, the downregulation of miRNAs involved in heart development in the healthy heart (e.g., mmu-miR-1a, mmu-miR-126a, and mmu-miR-342-5p; Figure S7E; Table S5) allows the upregulation of genes related to this process and to cardiac muscle contraction in CRMs (Figure 5B). The third subnetwork (S3) was controlled by miRNAs downregulated at day 7 and upregulated in CRMs (e.g., mmu-miR-484 and mmu-miR-345; Figure S7E; Table S5). Consistently with the functional analysis of genes in cluster III (Figure 1D), these miRNAs control genes predominantly related to ECM and collagen fibril organization (Figure 5B).

To further define the role of miRNAs in Mφ polarization, we focused on the comparison between 7 and 3 days post-injury (Table S4). miRNAs upregulated at day 3 (e.g., mmu-miR-301a, mmu-miR-425, and mmu-miR-155) supported the inflammatory response by potentially suppressing processes linked to cell surface receptor signaling pathway, tissue development,

Figure 4. Simulated Dynamics of Gene-Regulatory Network Reveals a Negative-Feedback Loop That Limits Initial Inflammation via Hypoxia-Mediated Upregulation of *Il10*

(A) Most significant active subnetwork. Nodes of the SCC of the module are highlighted in yellow.

(B–D) State 1 (B), 2 (C), and 3 (D) of the cycle attractor of the SCC network. Blue nodes are switched off, red nodes are on, and pink nodes oscillate between on/off states.

(E) mRNA expression levels of *Hif1a*, *Stat1*, and *Il10* were analyzed by qPCR in cardiac Mφs isolated at the indicated post-injury stages. Data are shown as mean ± SEM of three independent experiments; ***$p < 0.001$ (one-way ANOVA followed by Tukey test).

(F) mRNA expression of selected genes from the cycle attractor were tested by qPCR in *in vitro* peritoneal Mφs cultured for 24 hr in normoxia or hypoxia with or without IFN-γ treatment. Results are expressed as fold induction compared with control (normoxia). Data are mean ± SEM of three independent experiments; *$p < 0.05$, **$p < 0.01$, ***$p < 0.001$ versus control; $^{###}p < 0.001$ for hypoxia versus hypoxia plus IFN-γ (one-way ANOVA followed by Tukey test).

See also Figure S6.

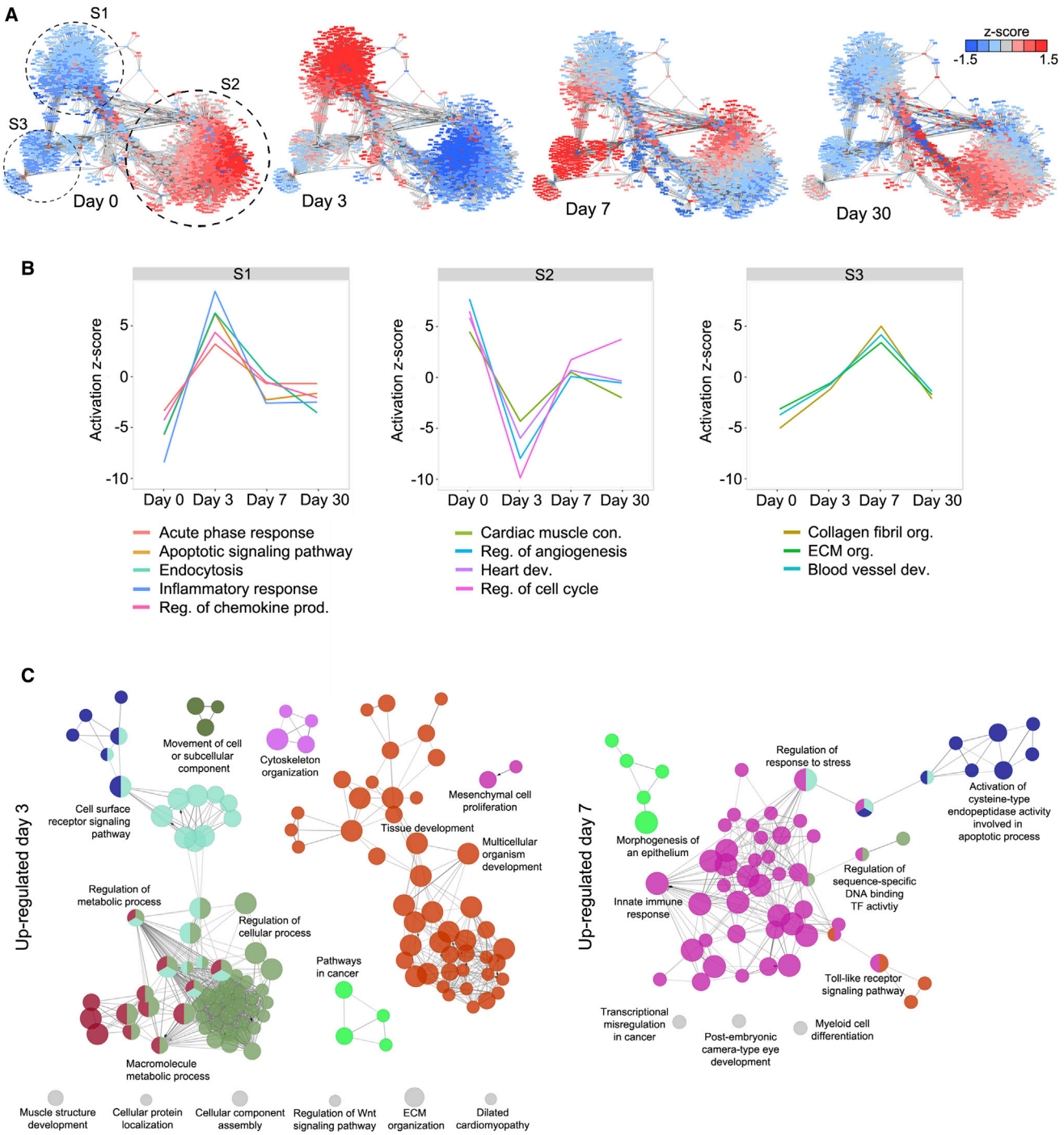

Figure 5. Analysis of the Cardiac Mφ miRnome in Healthy and Injured Hearts

(A) Global mRNA-miRNA interaction network. S1, S2, and S3 denote the three network clusters.

(B) Enriched biological processes associated with genes in the identified subnetworks.

(C) ClueGO network connecting the most significant functional terms (biological process or KEGG pathway) for the targets of those miRNAs significantly upregulated on day 3 (left) and on day 7 (right) post-injury. Colors represent different groups. For each group the most significant term is displayed. Con, contraction; dev, development; org, organization; prod, production; reg, regulation.

See also Figure S7 and Tables S4 and S5.

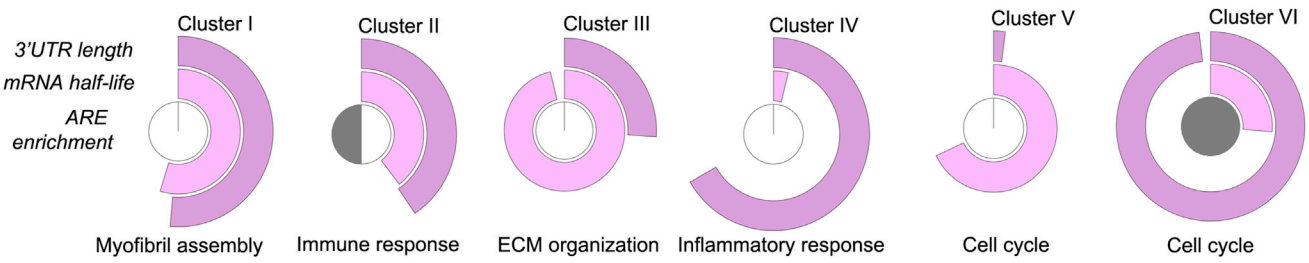

Figure 6. Analysis of mRNA Stability of Cardiac Mφs

Outer circle corresponds to median mRNA 3′-UTR length. Middle circle displays median mRNA half-life. Both values were normalized. Inner circle represents ARE enrichment: left side pentamer ("AUUUA") and right side heptamer ("UAUUUAU"). A white half-circle indicates no enrichment; gray indicates significant enrichment.

metabolism, and mesenchymal cell proliferation (Figure 5C). At 7 days post-injury, upregulated miRNAs (e.g., mmu-miR-125a, mmu-miR-146a, and mmu-miR-34a) might have contributed to resolution of inflammation by downregulating immune response-related genes (Figures 1C and 1D), facilitating the critical transition to an anti-inflammatory phenotype (Figure 5C). In addition, we found miRNAs potentially mediating silencing of apoptotic signaling pathways at day 7 (e.g., mmu-miR-133a, mmu-miR-146a, and mmu-miR-99a), consistent with the upregulation of cell proliferation genes at this stage (Figure 1D).

Specific Destabilization of Inflammatory mRNAs by the Activity of RNA-Binding Proteins

Other important players in post-transcriptional regulation are RNA-binding proteins (RBPs). To determine the possible regulatory effects of RBPs and miRNAs, we calculated the median length of 3′-UTRs per cluster (Figure 6). Median 3′-UTR length was highest for genes downregulated on days 3 (cluster VI) and 7 (cluster IV).

One upregulated RBP at 3 days post-injury was tristetraprolin (TTP) (symbol = *Zfp36*) (Figure 1C), which has been reported to destabilize a third of inflammation-induced unstable mRNAs in Mφs *in vitro* (Kratochvill et al., 2011). TTP binds to an AU-rich element (ARE) in the 3′-UTR of its target mRNAs. Testing of the k-means clusters for enrichment of AU-pentamers ("AUUUA") and AU-heptamers ("UAUUUAU") revealed significant upregulation of ARE-rich genes at 3 days post-injury (Figure 6), which, in combination with TTP upregulation (Figure 1C), indicates increased likelihood of TTP-directed regulation. We also found an enrichment of ARE-rich genes among the genes upregulated in the healthy heart and at 30 days post-injury (Figure 6). These genes were enriched for cell-cycle-related processes (Figure 1D), which is in line with the finding that many cell-cycle regulators are encoded by ARE-containing mRNAs (Barreau et al., 2006).

We next used mRNA degradation rates (Sharova et al., 2009) to calculate the median mRNA half-life of co-expressed genes. For all clusters, the median mRNA half-life anti-correlated with the median 3′-UTR length per cluster (spearman correlation coefficient = −0.82), indicating increased post-transcriptional regulation. In accordance with the results from the AU-motif enrichment analysis, the mRNAs in clusters II and VI had a half-life below the reported overall median of 7.1 hr. Genes downregulated 7 days post-injury (cluster IV) were not enriched for AU elements but had the shortest median mRNA half-life among all clusters (4.7 hr). This cluster was enriched for regulation of transcription (Table S2), which have been linked to unstable mRNAs (Sharova et al., 2009). Consistent with their shorter 3′-UTRs and lack of ARE enrichment (Figure 6), mRNAs from cluster III (day 7 post-injury) had a long median half-life (9.6 hr). This cluster was enriched for ECM organization and collagen fibril organization (Figures 1D and 6), structural processes associated with stable mRNAs.

Long Non-coding RNA Expression in Cardiac Mφs

Ensembl biotype information was used to classify DEGs as lincRNAs (Figure 7A; Table S6). lincRNAs and mRNA 3′-UTRs showed highly similar structural features (Figure 7B), but lincRNAs tended to have lower expression than mRNAs (Figure S7F).

We found that cluster IV had the highest relative abundance of lincRNAs (15.5%), including *Malat1* (Figures 7A and 7C), a lincRNA known to be induced by hypoxia and to play an important role in cardiovascular disease (CVD) (Skroblin and Mayr, 2014). In particular, *Malat1* has been reported to be increased in blood samples of MI patients versus healthy volunteers (Vausort et al., 2014). Within the same cluster, we found *Mir17hg* (Figure 7C), which encodes the miRNA 17-92 cluster. These miRNAs are associated with cell cycle and cell proliferation (Mogilyansky and Rigoutsos, 2013), indicating a potential role of *Mir17hg* in the regulation of Mφ proliferation. We found upregulation of *Neat1* at 3 days post-injury (cluster II, Figure 7C), which has been associated with the innate immune response (Imamura et al., 2014). This result agrees with the functional enrichment analysis of protein-coding genes linked to lincRNAs, showing that differential expression between days 0 and 3 was associated with processes related to antigen and leukocyte activation (Figure 7D). *Pvt1*, which has been proposed to function as a competing endogenous RNA (ceRNA) for MYC protein, preventing its degradation (Colombo et al., 2015), showed elevated expression in CRMs and at 30 days post-injury (Table S6).

Identification of all possible mRNA-lincRNA-miRNA triangles (Supplemental Experimental Procedures) revealed four different types of interaction (Figure 7E). The most abundant was characterized by positively correlated expression of all RNAs, among which we identified several triangles involving *Neat1* and *Pvt1*

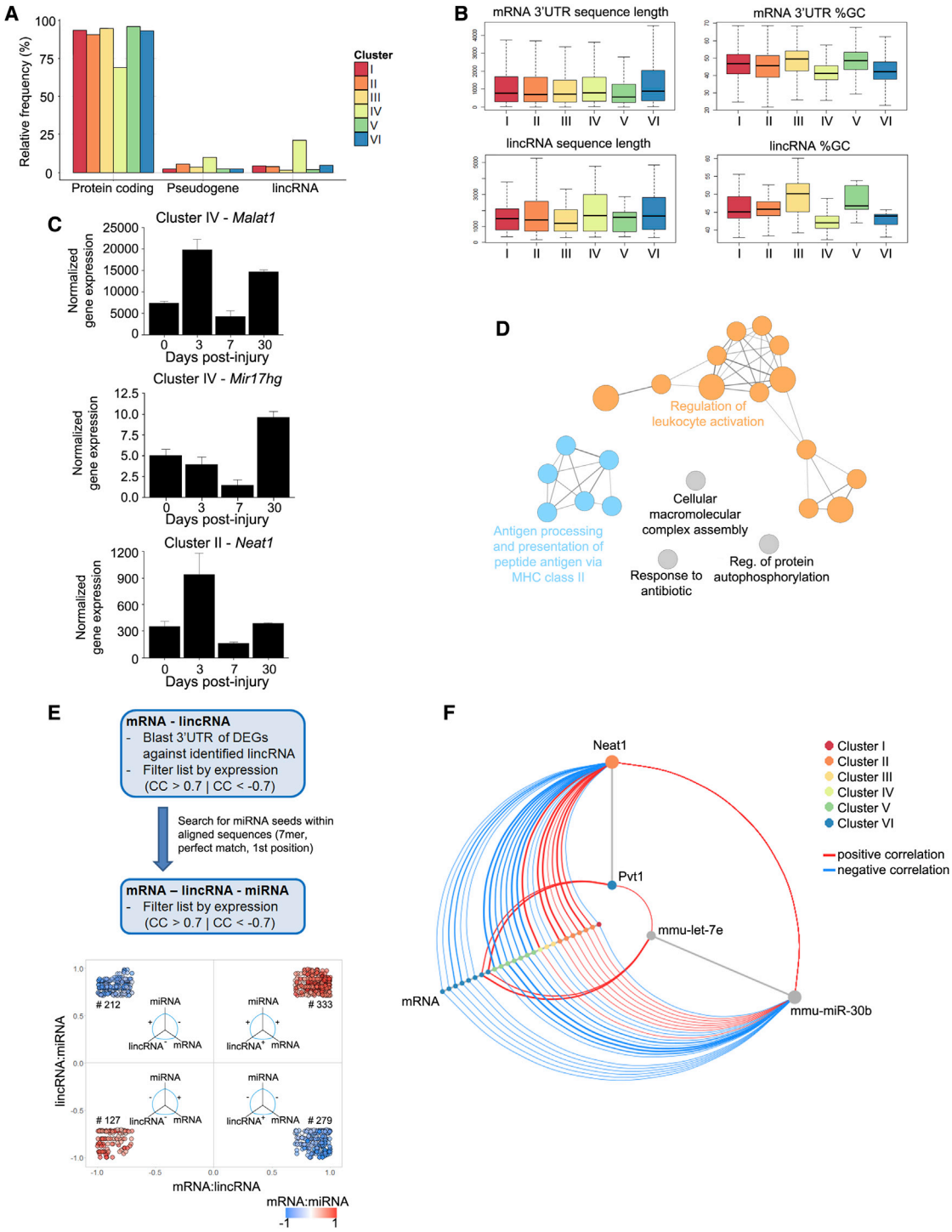

Figure 7. Analysis of lincRNAs in Cardiac Mφs

(A) Relative frequency of transcript biotypes per cluster.

(B) Structural similarities between mRNA 3′-UTR and lincRNA sequences.

(C) Normalized expression levels of selected lincRNAs measured by RNA-seq.

(D) ClueGO network connecting the most significant functional terms (biological process and KEGG pathway) for nearest genes of DE lincRNAs on day 3 versus day 0.

(E) Correlation of mRNA, lincRNA, and miRNA expression.

(F) Hive plot presentation of mRNA-lincRNA-miRNA triangle for the lincRNAs *Neat1* and *Pvt1*. Nodes representing lincRNAs and mRNAs are colored according to clusters. Red lines indicate positive correlation; blue lines indicate negative correlation.

See also Figure S7 and Table S6.

(Figure 7F). The identified mRNA-lincRNA-miRNA triangles including *Neat1* were linked through miR-30b, a miRNA associated with immune suppression (Gaziel-Sovran et al., 2011). The positive correlation between *Neat1*, miR-30b, and other immune response-related mRNAs may indicate that *Neat1* indirectly supports pro-inflammatory reactions as an additional binding partner for miR-30b, impairing the repressive effect of the miRNA.

DISCUSSION

In recent years, notable advances have been made in elucidating the origin of TRMs and their organ-specific gene and epigenetic signatures under steady-state conditions (Epelman et al., 2014; Fujiu et al., 2017; Ginhoux and Guilliams, 2016; Gosselin et al., 2014). However, Mφ activation after tissue injury *in vivo* remains poorly understood, mainly due to the lack of omics experiments with enough replication to achieve consistent conclusions (Yan et al., 2017). To address this issue, we have generated a global transcriptional dataset of mouse cardiac Mφs that captures the transcriptional changes (mRNA, miRNA, and lincRNA) of Mφs in the healthy heart and at various post-injury stages, providing an important resource for improving understanding of how Mφs integrate, process, and respond to signals from their local environment.

We first characterized the unique gene signature of CRMs. A previous comparison of Mφ transcriptional profiles in heart, spleen, and brain identified a set of 35 heart-specific Mφ genes (Pinto et al., 2012). However, our integrated analysis of mouse TRMs shows that although several genes of this signature are indeed specifically expressed in the heart, around 20% are expressed in both heart and intestine. The similar transcriptional profiles of mouse CRMs and intestinal Mφs possibly reflects a contribution to these populations from monocyte influx (Ginhoux and Guilliams, 2016). Cardiac-specific genes identified in our analysis include *Egfr*, *Lifr*, *Osmr*, and *Il1rl1*, which encode receptors involved in Mφ proliferation (Lamb et al., 2004), migration and chemotaxis (Sugiura et al., 2000), angiogenesis (Zhang et al., 2015), and the suppression of immune activity (Sweet et al., 2001). Remarkably, CRMs also showed specific expression of typical cardiomyocyte markers (*Myh6* and *Tnnt2*). Interestingly, *Myh6* expression has been reported in cardiac monocytes (Meyer et al., 2017). This finding could be a result of the environment instruction, as described for the microglia (Gosselin et al., 2017), but could also reflect the phagocytosis of dead cardiomyocytes by CRMs (Wan et al., 2013) to maintain cardiac homeostasis.

In line with previous reports (Hilgendorf et al., 2014; Nahrendorf et al., 2007), we identified distinct post-injury Mφ populations. The high plasticity of Mφs makes it difficult to identify population-specific surface markers, an essential requirement for targeted therapy. In line with Pinto et al. (2012), we found that CRMs highly express the hyaluronan receptor LYVE-1, suggesting a possible role in blood vessel development in the healthy heart (Cho et al., 2007). Since hyaluronan plays an important role in tissue integrity and cardiac-valve formation (Rodgers et al., 2006), LYVE-1 expression might indicate involvement of CRMs in these processes. We also found that CRMs express CD36, a scavenger receptor that mediates apoptotic cell intake to preserve cardiac homeostasis (Driscoll et al., 2013). Mφs at 3 days post-injury were characterized by CD40 and CD274 expression, indicating further amplification of the inflammatory response by T cell activation via CD40:CD154 interactions (Suttles and Stout, 2009) and subsequent modulation of T cell responses (Sharpe et al., 2007). MRC1 was highly expressed in CRMs in the healthy heart and was then downregulated during the inflammatory phase, recovering its expression from 7 days post-injury. By 30 days post-injury, its expression returned to the level in CRMs, suggesting MRC1 as a possible marker of homeostasis restoration in post-injury Mφs.

Our RNA-seq analysis reveals massive changes in the cardiac Mφ transcriptome at 3 days post-injury, likely due to the large influx of monocyte-derived Ly6C^{high}/CX3CR1^{low} Mφs (Heidt et al., 2014; Hilgendorf et al., 2014). These changes were associated with an immune response primarily triggered by IFN-γ and STAT1 signaling. However, *Ifnγ* was not upregulated in post-injury Mφs, suggesting its production by other cell types such as T cells and natural killer (NK) cells (Knorr et al., 2014). Our data further suggest that Mφs sustain their activation at this post-injury stage by secreting pro-inflammatory cytokines, with the potential for autocrine signaling. During the reparative phase, Mφs were characterized by an extensive secretome mainly composed of angiogenic and ECM-related components, indicating the pivotal role of Mφs in angiogenesis and tissue remodeling (Lambert et al., 2008). The high similarity in gene expression between CRMs and 30-day post-injury Mφs indicates progressive deactivation after the inflammatory phase and a restoration of homeostasis. However, functional analysis revealed a lack of heart development reactivation at 30 days post-injury, possibly reflecting the prolonged miRNA-mediated suppression of involved genes. Our data provide the basis for future studies aimed at defining the differences between naive resident Mφs and the long-lived monocyte-derived cells that replace them after tissue injury.

In vitro studies of Mφ plasticity have produced an oversimplified binary M1/M2 classification (Sica et al., 2015) that has limited ability to explain the plethora of phenotypes observed *in vivo* (Novak et al., 2014; Varga et al., 2016). Partial deconvolution revealed that Mφs involved in cardiac repair are hybrids of the phenotypes described *in vitro*, characterized by mixed expression of M1/M2 polarization programs. This finding is consistent with the idea that activated Mφs occur as a continuum rather than as discrete entities (Novak et al., 2014; Varga et al., 2016). This could reflect heterogeneity within the population or co-expression of M1/M2 markers by the same cell. Further studies at single-cell level would be required to address this issue. Our analysis further indicates that post-injury Mφs dynamically shift their phenotype to orchestrate cardiac repair. A detailed understanding of this phenotypic transition is essential for developing timed interventions to improve cardiac healing (Harel-Adar et al., 2011).

Mφ deactivation after sterile tissue injury is orchestrated by extrinsic and intrinsic control mechanisms, with IL-10 being the dominant mediator of the anti-inflammatory program in Mφs (Lambert et al., 2008). We detected elevated *Il10* expression as early as 3 days post-injury, in line with previous findings in injured muscle (Novak et al., 2014). Network modeling of the regulatory

core of post-injury Mφs revealed a cycle attractor mainly characterized by oscillations in *Hif1a*, *Stat1*, and *Il10* activation. Validation *in vitro* showed that *Il10* is upregulated under hypoxic conditions, indicating either hypoxia-mediated *Il10* induction (Cai et al., 2013) or stabilization of *Il10* mRNA (Powell et al., 2000). This upregulation is most likely followed by IL-10-mediated auto-regulation (Sarkar et al., 2008). Our data support the idea that the transition from the pro-inflammatory to the anti-inflammatory phenotype *in vivo* is conditioned not only by the tissue microenvironment, but also by cell-intrinsic factors.

We also detected post-transcriptional regulation of Mφ deactivation. Our *in silico* mRNA stability analysis supports the finding that inflammation-induced mRNAs are less stable (Kratochvill et al., 2011) due to their longer 3′-UTRs enriched in AREs, the binding element for TTP. Moreover, we found that miRNAs potentially control immune response-related genes and that, while TTP-driven mRNA decay occurs in response to induced inflammation, the suppression of inflammation in the healthy heart may also involve a contribution from miRNA activity. We also found that miRNAs potentially downregulate cell proliferation during the inflammatory phase, whereas with the resolution of inflammation Mφs regain the ability to proliferate (Varga et al., 2016). Together, the enrichment in inflammatory-related mRNAs with longer and ARE-enriched 3′-UTR regions, the increase in lincRNAs, and the lack of TFs specific to cluster IV suggest post-transcriptional regulation of these genes.

In recent years, multiple lincRNAs have been linked to the immune response and CVD (Skroblin and Mayr, 2014), but it remains unclear how these molecules act within cells. Based on the ceRNA hypothesis (Salmena et al., 2011), we identified several mRNA-lincRNA-miRNA motifs. One of these motifs may indicate that *Neat1* indirectly supports pro-inflammatory reactions as an additional binding partner for the immune-suppressive miRNA miR-30b, which is induced by a hypoxic environment (Choudhry and Mole, 2016). Targeted deletion studies will be needed to assess the specific functions of altered lincRNAs involved in Mφ activation.

In summary, our study provides insight into Mφ signal processing and transcriptional regulation in the healthy heart and at different stages post-injury. We anticipate that this dataset will serve as a resource for elucidating the role of CRMs and as a starting point for Mφ-based therapies to improve cardiac repair. Moreover, this dataset also has potential to identify novel targets for miRNA-based therapy and to elucidate the function and regulatory impact of activated lincRNAs.

EXPERIMENTAL PROCEDURES

Detailed description of experimental procedures and bioinformatics analysis are provided in Supplemental Experimental Procedures.

Mice and Myocardial Injury Model

Two- to 3-month-old male and female $CX_3CR1^{GFP/+}$ (Jung et al., 2000) and C57BL/6 mice (Charles River) were used. All animal procedures were conducted in accordance with European Union (EU) Directive 2010/526/EC, enforced in Spanish law under Real Decreto 53/2013. Cryoinjury was induced as previously described (van Amerongen et al., 2008). Animals were sacrificed on days 3, 7, and 30 post-injury, and hearts were isolated. Animals not subjected to surgery were included as the physiological condition (day 0).

Cell Sorting and RNA Isolation

Single-cell suspensions were sorted with a BD FACSAria II cell sorter (BD Biosciences) using the gating strategy shown in Figures S2A, S2B, S5B, and S5C. Total RNA was isolated using the miRNeasy Micro Kit (QIAGEN). RNA quality and quantity were measured using the 2100 Bioanalyzer (Agilent Technologies).

RNA-Seq

For RNA-seq, total RNA was reverse transcribed and amplified using the Ovation RNA-Seq System V2 (NuGEN). Amplified cDNA was sonicated to 100- to 300-bp fragments and used with the TruSeq DNA Sample Preparation, Version 2, Kit (Illumina) to generate index-tagged sequencing libraries. Libraries were analyzed in a 2100 Bioanalyzer (Agilent Technologies) and then sequenced in a Genome Analyzer IIx (Illumina) to generate single 75-bp reads.

Microarrays

Total RNA was labeled using the miRNA Microarray System with miRNA Complete Labeling and Hyb Kit (Agilent Technologies), and then hybridized to SurePrint G3 Mouse miRNA Microarray slides (release 19.0) containing 1,247 mouse mature miRNA probes (Agilent Technologies).

Partial Deconvolution Analysis

The R package CellMix (Gaujoux and Seoighe, 2013) was used for *in silico* gene expression deconvolution analysis. Partial deconvolution of gene expression from Mφs isolated at various post-injury stages was performed using the *in vivo* control sample (CRMs) and *in vitro* derived M1 (BMDMs activated with LPS plus IFN-γ) and M2 (BMDMs activated with IL-4 plus IL-13) specific signature profiles downloaded from GSE53321 (Li et al., 2015). Data were normalized, log transformed, and adjusted for batch effects using the comBat function implemented in the R package sva (Leek et al., 2012).

Transcriptional Networks

Pathway analysis was performed with PathVisio (Kutmon et al., 2015). The mouse pathway collection from WikiPathways (Kelder et al., 2012) was used to perform an over-representation analysis with the transcriptomics dataset. The pathways were ranked based on a standardized difference score (z score). Pathways with a z score > 2.0, p value < 0.05, and minimum of four measured genes were considered significant. Enriched pathways were imported as networks into cytoscape using the WikiPathways app and the top ten most significant pathways were subsequently merged into a PKN (Rodriguez et al., 2015). The PKN was further extended with protein-protein interactions (first neighbors) extracted from Ingenuity software (https://www.ingenuity.com/) between the genes in the pathways and DEGs. The jActiveModules cytoscape app (Ideker et al., 2002) was used to identify active modules within the molecular interaction network. For the highest scoring active module, SCCs were calculated using the BiNoM app (Zinovyev et al., 2008). In the mathematical theory of graphs, a graph is strongly connected if there is a path between all pairs of vertices. BoolSim software was used to identify attractors of the SCC network (Garg et al., 2009).

DATA AND SOFTWARE AVAILABILITY

The accession number for the raw and processed sequencing data reported in this study is GEO: GSE97147.

SUPPLEMENTAL INFORMATION

Supplemental Information includes Supplemental Experimental Procedures, seven figures, and six tables and can be found with this article online at https://doi.org/10.1016/j.celrep.2018.03.029.

ACKNOWLEDGMENTS

We thank S. Bartlett (CNIC) for editorial assistance and the CNIC Cellomics and Genomics Units for technical help. This work was supported by grants from the Spanish Ministry of Economy and Competitiveness (SAF2015-64287R and SAF2015-71878-REDT) to M.R., and Fundación Marató TV3

(121931) and the European Commission FP7 (CardioNext-ITN-608027) to M.R. and A.G.A. L.A.-H. is funded by a fellowship from La Caixa-CNIC. The CNIC is supported by MEIC and the Pro CNIC Foundation, and is a Severo Ochoa Center of Excellence (MEIC award SEV-2015-0505).

AUTHOR CONTRIBUTIONS

L.A.-H., V.T., M.C., A.K., and V.N. performed experiments. L.A.-H., V.T., and M.C. analyzed experimental data. W.W. and F.S.-C. performed bioinformatics analysis. W.W. and I.C. performed network analysis. W.W. and M.I. performed lincRNA analysis. A.G.A. and I.X. provided critical suggestions. W.W., L.A.-H., F.S.-C., and M.R. wrote the manuscript. F.S.-C. designed the bioinformatics analysis strategy. M.R. conceived and designed the project and experiments.

DECLARATION OF INTERESTS

The authors declare no competing interests.

Received: November 15, 2017
Revised: February 5, 2018
Accepted: March 7, 2018
Published: April 10, 2018

REFERENCES

Albert, R. (2007). Network inference, analysis, and modeling in systems biology. Plant Cell *19*, 3327–3338.

Barreau, C., Paillard, L., and Osborne, H.B. (2006). AU-rich elements and associated factors: are there unifying principles? Nucleic Acids Res. *33*, 7138–7150.

Braun, D.A., Fribourg, M., and Sealfon, S.C. (2013). Cytokine response is determined by duration of receptor and signal transducers and activators of transcription 3 (STAT3) activation. J. Biol. Chem. *288*, 2986–2993.

Cai, Z., Luo, W., Zhan, H., and Semenza, G.L. (2013). Hypoxia-inducible factor 1 is required for remote ischemic preconditioning of the heart. Proc. Natl. Acad. Sci. USA *110*, 17462–17467.

Cho, C.H., Koh, Y.J., Han, J., Sung, H.K., Jong Lee, H., Morisada, T., Schwendener, R.A., Brekken, R.A., Kang, G., Oike, Y., et al. (2007). Angiogenic role of LYVE-1-positive macrophages in adipose tissue. Circ. Res. *100*, e47–e57.

Choudhry, H., and Mole, D.R. (2016). Hypoxic regulation of the noncoding genome and NEAT1. Brief. Funct. Genomics *15*, 174–185.

Colombo, T., Farina, L., Macino, G., and Paci, P. (2015). PVT1: a rising star among oncogenic long noncoding RNAs. BioMed Res. Int. *2015*, 304208.

Davies, L.C., Jenkins, S.J., Allen, J.E., and Taylor, P.R. (2013). Tissue-resident macrophages. Nat. Immunol. *14*, 986–995.

Driscoll, W.S., Vaisar, T., Tang, J., Wilson, C.L., and Raines, E.W. (2013). Macrophage ADAM17 deficiency augments CD36-dependent apoptotic cell uptake and the linked anti-inflammatory phenotype. Circ. Res. *113*, 52–61.

Epelman, S., Lavine, K.J., Beaudin, A.E., Sojka, D.K., Carrero, J.A., Calderon, B., Brija, T., Gautier, E.L., Ivanov, S., Satpathy, A.T., et al. (2014). Embryonic and adult-derived resident cardiac macrophages are maintained through distinct mechanisms at steady state and during inflammation. Immunity *40*, 91–104.

Fujiu, K., Shibata, M., Nakayama, Y., Ogata, F., Matsumoto, S., Noshita, K., Iwami, S., Nakae, S., Komuro, I., Nagai, R., and Manabe, I. (2017). A heart-brain-kidney network controls adaptation to cardiac stress through tissue macrophage activation. Nat. Med. *23*, 611–622.

Garg, A., Mohanram, K., Di Cara, A., De Micheli, G., and Xenarios, I. (2009). Modeling stochasticity and robustness in gene regulatory networks. Bioinformatics *25*, i101–i109.

Gaujoux, R., and Seoighe, C. (2013). CellMix: a comprehensive toolbox for gene expression deconvolution. Bioinformatics *29*, 2211–2212.

Gautier, E.L., Shay, T., Miller, J., Greter, M., Jakubzick, C., Ivanov, S., Helft, J., Chow, A., Elpek, K.G., Gordonov, S., et al.; Immunological Genome Consortium (2012). Gene-expression profiles and transcriptional regulatory pathways that underlie the identity and diversity of mouse tissue macrophages. Nat. Immunol. *13*, 1118–1128.

Gaziel-Sovran, A., Segura, M.F., Di Micco, R., Collins, M.K., Hanniford, D., Vega-Saenz de Miera, E., Rakus, J.F., Dankert, J.F., Shang, S., Kerbel, R.S., et al. (2011). miR-30b/30d regulation of GalNAc transferases enhances invasion and immunosuppression during metastasis. Cancer Cell *20*, 104–118.

Ginhoux, F., and Guilliams, M. (2016). Tissue-resident macrophage ontogeny and homeostasis. Immunity *44*, 439–449.

Glass, C.K., and Saijo, K. (2010). Nuclear receptor transrepression pathways that regulate inflammation in macrophages and T cells. Nat. Rev. Immunol. *10*, 365–376.

Gosselin, D., Link, V.M., Romanoski, C.E., Fonseca, G.J., Eichenfield, D.Z., Spann, N.J., Stender, J.D., Chun, H.B., Garner, H., Geissmann, F., and Glass, C.K. (2014). Environment drives selection and function of enhancers controlling tissue-specific macrophage identities. Cell *159*, 1327–1340.

Gosselin, D., Skola, D., Coufal, N.G., Holtman, I.R., Schlachetzki, J.C.M., Sajti, E., Jaeger, B.N., O'Connor, C., Fitzpatrick, C., Pasillas, M.P., et al. (2017). An environment-dependent transcriptional network specifies human microglia identity. Science *356*, eaal3222.

Harel-Adar, T., Ben Mordechai, T., Amsalem, Y., Feinberg, M.S., Leor, J., and Cohen, S. (2011). Modulation of cardiac macrophages by phosphatidylserine-presenting liposomes improves infarct repair. Proc. Natl. Acad. Sci. USA *108*, 1827–1832.

Heidt, T., Courties, G., Dutta, P., Sager, H.B., Sebas, M., Iwamoto, Y., Sun, Y., Da Silva, N., Panizzi, P., van der Laan, A.M., et al. (2014). Differential contribution of monocytes to heart macrophages in steady-state and after myocardial infarction. Circ. Res. *115*, 284–295.

Hilgendorf, I., Gerhardt, L.M., Tan, T.C., Winter, C., Holderried, T.A., Chousterman, B.G., Iwamoto, Y., Liao, R., Zirlik, A., Scherer-Crosbie, M., et al. (2014). Ly-6Chigh monocytes depend on Nr4a1 to balance both inflammatory and reparative phases in the infarcted myocardium. Circ. Res. *114*, 1611–1622.

Hu, X., Paik, P.K., Chen, J., Yarilina, A., Kockeritz, L., Lu, T.T., Woodgett, J.R., and Ivashkiv, L.B. (2006). IFN-γ suppresses IL-10 production and synergizes with TLR2 by regulating GSK3 and CREB/AP-1 proteins. Immunity *24*, 563–574.

Hulsmans, M., Clauss, S., Xiao, L., Aguirre, A.D., King, K.R., Hanley, A., Hucker, W.J., Wülfers, E.M., Seemann, G., Courties, G., et al. (2017). Macrophages facilitate electrical conduction in the heart. Cell *169*, 510–522.e20.

Ideker, T., Ozier, O., Schwikowski, B., and Siegel, A.F. (2002). Discovering regulatory and signalling circuits in molecular interaction networks. Bioinformatics *18* (*Suppl 1*), S233–S240.

Imamura, K., Imamachi, N., Akizuki, G., Kumakura, M., Kawaguchi, A., Nagata, K., Kato, A., Kawaguchi, Y., Sato, H., Yoneda, M., et al. (2014). Long noncoding RNA NEAT1-dependent SFPQ relocation from promoter region to paraspeckle mediates IL8 expression upon immune stimuli. Mol. Cell *53*, 393–406.

Jung, S., Aliberti, J., Graemmel, P., Sunshine, M.J., Kreutzberg, G.W., Sher, A., and Littman, D.R. (2000). Analysis of fractalkine receptor CX_3CR1 function by targeted deletion and green fluorescent protein reporter gene insertion. Mol. Cell. Biol. *20*, 4106–4114.

Kaelin, W.G., Jr., and Ratcliffe, P.J. (2008). Oxygen sensing by metazoans: the central role of the HIF hydroxylase pathway. Mol. Cell *30*, 393–402.

Kelder, T., van Iersel, M.P., Hanspers, K., Kutmon, M., Conklin, B.R., Evelo, C.T., and Pico, A.R. (2012). WikiPathways: building research communities on biological pathways. Nucleic Acids Res *40*, D1301–D1307.

Knorr, M., Münzel, T., and Wenzel, P. (2014). Interplay of NK cells and monocytes in vascular inflammation and myocardial infarction. Front. Physiol. *5*, 295.

Kratochvill, F., Machacek, C., Vogl, C., Ebner, F., Sedlyarov, V., Gruber, A.R., Hartweger, H., Vielnascher, R., Karaghiosoff, M., Rülicke, T., et al. (2011). Tristetraprolin-driven regulatory circuit controls quality and timing of mRNA decay in inflammation. Mol. Syst. Biol. *7*, 560.

Kutmon, M., van Iersel, M.P., Bohler, A., Kelder, T., Nunes, N., Pico, A.R., and Evelo, C.T. (2015). PathVisio 3: an extendable pathway analysis toolbox. PLoS Comput. Biol *11*, e1004085.

Lamb, D.J., Modjtahedi, H., Plant, N.J., and Ferns, G.A. (2004). EGF mediates monocyte chemotaxis and macrophage proliferation and EGF receptor is expressed in atherosclerotic plaques. Atherosclerosis *176*, 21–26.

Lambert, J.M., Lopez, E.F., and Lindsey, M.L. (2008). Macrophage roles following myocardial infarction. Int. J. Cardiol. *130*, 147–158.

Lavin, Y., Winter, D., Blecher-Gonen, R., David, E., Keren-Shaul, H., Merad, M., Jung, S., and Amit, I. (2014). Tissue-resident macrophage enhancer landscapes are shaped by the local microenvironment. Cell *159*, 1312–1326.

Leek, J.T., Johnson, W.E., Parker, H.S., Jaffe, A.E., and Storey, J.D. (2012). The sva package for removing batch effects and other unwanted variation in high-throughput experiments. Bioinformatics *28*, 882–883.

Li, L., Ng, D.S., Mah, W.C., Almeida, F.F., Rahmat, S.A., Rao, V.K., Leow, S.C., Laudisi, F., Peh, M.T., Goh, A.M., et al. (2015). A unique role for p53 in the regulation of M2 macrophage polarization. Cell Death Differ. *22*, 1081–1093.

Meyer, I.S., Jungmann, A., Dieterich, C., Zhang, M., Lasitschka, F., Werkmeister, S., Haas, J., Müller, O.J., Boutros, M., Nahrendorf, M., et al. (2017). The cardiac microenvironment uses non-canonical WNT signaling to activate monocytes after myocardial infarction. EMBO Mol. Med. *9*, 1279–1293.

Mogilyansky, E., and Rigoutsos, I. (2013). The miR-17/92 cluster: a comprehensive update on its genomics, genetics, functions and increasingly important and numerous roles in health and disease. Cell Death Differ. *20*, 1603–1614.

Nahrendorf, M., Swirski, F.K., Aikawa, E., Stangenberg, L., Wurdinger, T., Figueiredo, J.L., Libby, P., Weissleder, R., and Pittet, M.J. (2007). The healing myocardium sequentially mobilizes two monocyte subsets with divergent and complementary functions. J. Exp. Med. *204*, 3037–3047.

Novak, M.L., Weinheimer-Haus, E.M., and Koh, T.J. (2014). Macrophage activation and skeletal muscle healing following traumatic injury. J. Pathol. *232*, 344–355.

Pearce, E.L., Mullen, A.C., Martins, G.A., Krawczyk, C.M., Hutchins, A.S., Zediak, V.P., Banica, M., DiCioccio, C.B., Gross, D.A., Mao, C.A., et al. (2003). Control of effector $CD8^+$ T cell function by the transcription factor Eomesodermin. Science *302*, 1041–1043.

Pinto, A.R., Paolicelli, R., Salimova, E., Gospocic, J., Slonimsky, E., Bilbao-Cortes, D., Godwin, J.W., and Rosenthal, N.A. (2012). An abundant tissue macrophage population in the adult murine heart with a distinct alternatively-activated macrophage profile. PLoS One *7*, e36814.

Powell, M.J., Thompson, S.A., Tone, Y., Waldmann, H., and Tone, M. (2000). Posttranscriptional regulation of IL-10 gene expression through sequences in the 3′-untranslated region. J. Immunol. *165*, 292–296.

Rhinn, M., and Dollé, P. (2012). Retinoic acid signalling during development. Development *139*, 843–858.

Rodgers, L.S., Lalani, S., Hardy, K.M., Xiang, X., Broka, D., Antin, P.B., and Camenisch, T.D. (2006). Depolymerized hyaluronan induces vascular endothelial growth factor, a negative regulator of developmental epithelial-to-mesenchymal transformation. Circ. Res. *99*, 583–589.

Rodriguez, A., Crespo, I., Androsova, G., and del Sol, A. (2015). Discrete logic modelling optimization to contextualize prior knowledge networks using PRUNET. PLoS One *10*, e0127216.

Rusinova, I., Forster, S., Yu, S., Kannan, A., Masse, M., Cumming, H., Chapman, R., and Hertzog, P.J. (2013). Interferome v2.0: an updated database of annotated interferon-regulated genes. Nucleic Acids Res. *41*, D1040–D1046.

Salmena, L., Poliseno, L., Tay, Y., Kats, L., and Pandolfi, P.P. (2011). A ceRNA hypothesis: the Rosetta Stone of a hidden RNA language? Cell *146*, 353–358.

Sarkar, S., Sinsimer, K.S., Foster, R.L., Brewer, G., and Pestka, S. (2008). AUF1 isoform-specific regulation of anti-inflammatory IL10 expression in monocytes. J. Interferon Cytokine Res. *28*, 679–691.

Sharova, L.V., Sharov, A.A., Nedorezov, T., Piao, Y., Shaik, N., and Ko, M.S. (2009). Database for mRNA half-life of 19 977 genes obtained by DNA microarray analysis of pluripotent and differentiating mouse embryonic stem cells. DNA Res. *16*, 45–58.

Sharpe, A.H., Wherry, E.J., Ahmed, R., and Freeman, G.J. (2007). The function of programmed cell death 1 and its ligands in regulating autoimmunity and infection. Nat. Immunol. *8*, 239–245.

Shen-Orr, S.S., Tibshirani, R., Khatri, P., Bodian, D.L., Staedtler, F., Perry, N.M., Hastie, T., Sarwal, M.M., Davis, M.M., and Butte, A.J. (2010). Cell type-specific gene expression differences in complex tissues. Nat. Methods *7*, 287–289.

Sica, A., Erreni, M., Allavena, P., and Porta, C. (2015). Macrophage polarization in pathology. Cell. Mol. Life Sci. *72*, 4111–4126.

Skroblin, P., and Mayr, M. (2014). "Going long": long non-coding RNAs as biomarkers. Circ. Res. *115*, 607–609.

Sugiura, S., Lahav, R., Han, J., Kou, S.Y., Banner, L.R., de Pablo, F., and Patterson, P.H. (2000). Leukaemia inhibitory factor is required for normal inflammatory responses to injury in the peripheral and central nervous systems in vivo and is chemotactic for macrophages in vitro. Eur. J. Neurosci. *12*, 457–466.

Suttles, J., and Stout, R.D. (2009). Macrophage CD40 signaling: a pivotal regulator of disease protection and pathogenesis. Semin. Immunol. *21*, 257–264.

Sweet, M.J., Leung, B.P., Kang, D., Sogaard, M., Schulz, K., Trajkovic, V., Campbell, C.C., Xu, D., and Liew, F.Y. (2001). A novel pathway regulating lipopolysaccharide-induced shock by ST2/T1 via inhibition of Toll-like receptor 4 expression. J. Immunol. *166*, 6633–6639.

Swirski, F.K., Nahrendorf, M., Etzrodt, M., Wildgruber, M., Cortez-Retamozo, V., Panizzi, P., Figueiredo, J.L., Kohler, R.H., Chudnovskiy, A., Waterman, P., et al. (2009). Identification of splenic reservoir monocytes and their deployment to inflammatory sites. Science *325*, 612–616.

Takeda, N., O'Dea, E.L., Doedens, A., Kim, J.W., Weidemann, A., Stockmann, C., Asagiri, M., Simon, M.C., Hoffmann, A., and Johnson, R.S. (2010). Differential activation and antagonistic function of HIF-α isoforms in macrophages are essential for NO homeostasis. Genes Dev. *24*, 491–501.

Tooze, R.M., Stephenson, S., and Doody, G.M. (2006). Repression of IFN-γ induction of class II transactivator: a role for PRDM1/Blimp-1 in regulation of cytokine signaling. J. Immunol. *177*, 4584–4593.

van Amerongen, M.J., Harmsen, M.C., Petersen, A.H., Popa, E.R., and van Luyn, M.J.A. (2008). Cryoinjury: a model of myocardial regeneration. Cardiovasc. Pathol. *17*, 23–31.

Varga, T., Mounier, R., Horvath, A., Cuvellier, S., Dumont, F., Poliska, S., Ardjoune, H., Juban, G., Nagy, L., and Chazaud, B. (2016). Highly dynamic transcriptional signature of distinct macrophage subsets during sterile inflammation, resolution, and tissue repair. J. Immunol. *196*, 4771–4782.

Vausort, M., Wagner, D.R., and Devaux, Y. (2014). Long noncoding RNAs in patients with acute myocardial infarction. Circ. Res. *115*, 668–677.

Wan, E., Yeap, X.Y., Dehn, S., Terry, R., Novak, M., Zhang, S., Iwata, S., Han, X., Homma, S., Drosatos, K., et al. (2013). Enhanced efferocytosis of apoptotic cardiomyocytes through myeloid-epithelial-reproductive tyrosine kinase links acute inflammation resolution to cardiac repair after infarction. Circ. Res. *113*, 1004–1012.

Yan, X., Zhang, H., Fan, Q., Hu, J., Tao, R., Chen, Q., Iwakura, Y., Shen, W., Lu, L., Zhang, Q., and Zhang, R. (2017). Dectin-2 deficiency modulates Th1 differentiation and improves wound healing after myocardial infarction. Circ. Res. *120*, 1116–1129.

Yu, R.Y.-L., Wang, X., Pixley, F.J., Yu, J.J., Dent, A.L., Broxmeyer, H.E., Stanley, E.R., and Ye, B.H. (2005). BCL-6 negatively regulates macrophage proliferation by suppressing autocrine IL-6 production. Blood *105*, 1777–1784.

Zhang, X., Zhu, D., Wei, L., Zhao, Z., Qi, X., Li, Z., and Sun, D. (2015). OSM enhances angiogenesis and improves cardiac function after myocardial infarction. BioMed Res. Int. *2015*, 317905.

Zinovyev, A., Viara, E., Calzone, L., and Barillot, E. (2008). BiNoM: a Cytoscape plugin for manipulating and analyzing biological networks. Bioinformatics *24*, 876–877.

Cell Reports, Volume *23*

Supplemental Information

Deciphering the Dynamic Transcriptional and Post-transcriptional Networks of Macrophages in the Healthy Heart and after Myocardial Injury

Wencke Walter, Laura Alonso-Herranz, Verdiana Trappetti, Isaac Crespo, Mark Ibberson, Marta Cedenilla, Anna Karaszewska, Vanessa Núñez, Ioannis Xenarios, Alicia G. Arroyo, Fátima Sánchez-Cabo, and Mercedes Ricote

SUPPLEMENTAL INFORMATION

Supplemental Figures and legends

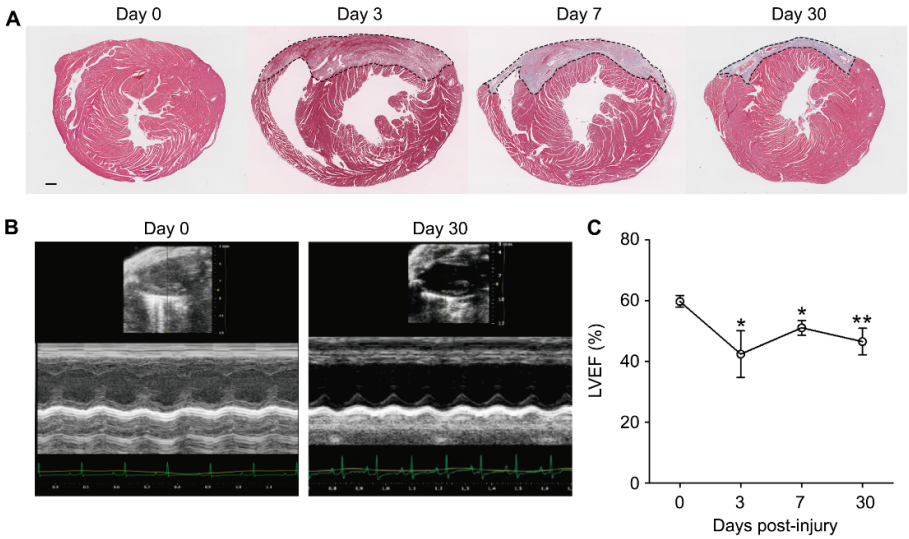

Figure S1. Cryoinjury as model to induce myocardial damage. Related to Figure 1.
(A) Representative images (whole heart, Scale bar=1mm) of Masson's Trichrome stained transversal sections of cryoinjured hearts at 0, 3, 7 and 30 days post-injury. Dashed lines depict the lesion. (B) Representative two dimensional and corresponding M-mode images of a long-axis view at 0 and 30 days post-injury. (C) Left ventricle ejection fraction (LVEF) was measured by *in vivo* 2D echocardiography analysis using the area-length method from long-axis view at 0 and 30 days post-injury. Data represent the mean ± SEM of 4-8 mice *per* group. Significant differences compared to healthy hearts are indicated as *p<0.05, **p<0.01.

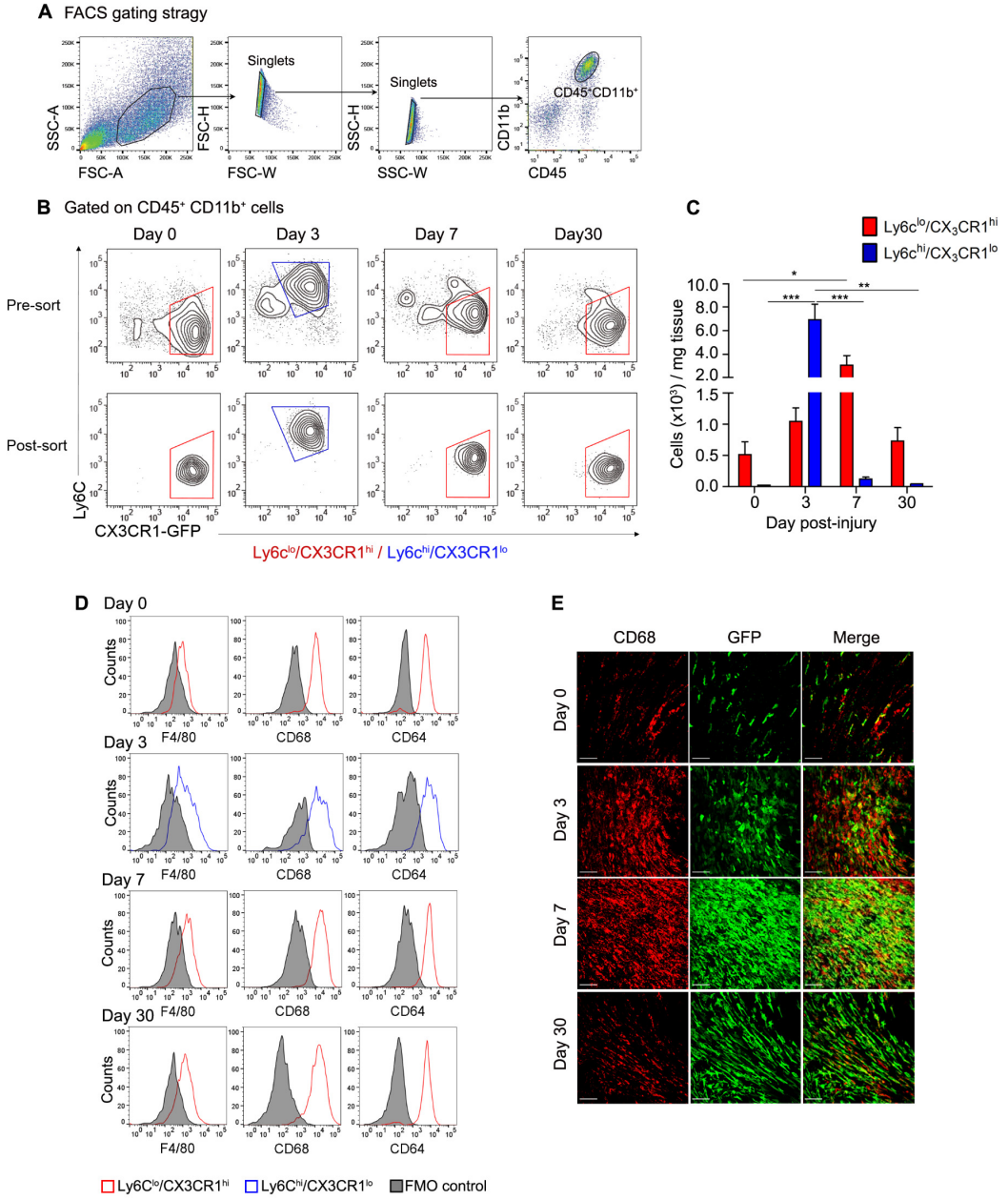

Figure S2. Characterization and isolation of cardiac Mφs in $CX_3CR1^{GFP/+}$ mice after cryoinjury. Related to Figure 1.

(A) FACS gating strategy to purify cardiac Mφs at different post-injury stages. (B) Within the $CD45^+$ $CD11b^+$ cells, the $Ly6C^{low}/CX_3CR1^{high}$ population (red) was sorted for 0, 7, and 30 days post-injury. The $Ly6C^{high}/CX_3CR1^{low}$ population (blue) was purified for 3 days post-injury. Representative post-sort of Mφs at 0, 3, 7, and 30 days post-injury are shown in the bottom panel. Sorting was performed with a pool of 5-10 mice per time point. (C) Total number of $Ly6C^{low}/CX_3CR1^{high}$ (red) and $Ly6C^{high}/CX_3CR1^{low}$ (blue) cells per mg of tissue at 0, 3, 7, and 30 days post-injury. Data represent the mean ± SEM of 4-5 mice; *P<0.05, **P<0.01, ***P<0.001 (One way-ANOVA followed by Tukey test). (D) Immunophenotype of $Ly6C^{low}/CX_3CR1^{high}$ population (red) and $Ly6C^{high}/CX_3CR1^{low}$ population (blue). The selected populations at 0, 3, 7, and 30 days post-injury were analyzed for the expression of F4/80, CD68, and CD64. Representative histograms depict the staining for the indicated antibodies. FMO is used as control. (E) Representative images of 30µm maximum intensity projection of cardiac

Mφs labeled with GFP (green) and CD68 (red) from $CX_3CR1^{GFP/+}$ mouse hearts at the indicated days post-injury.

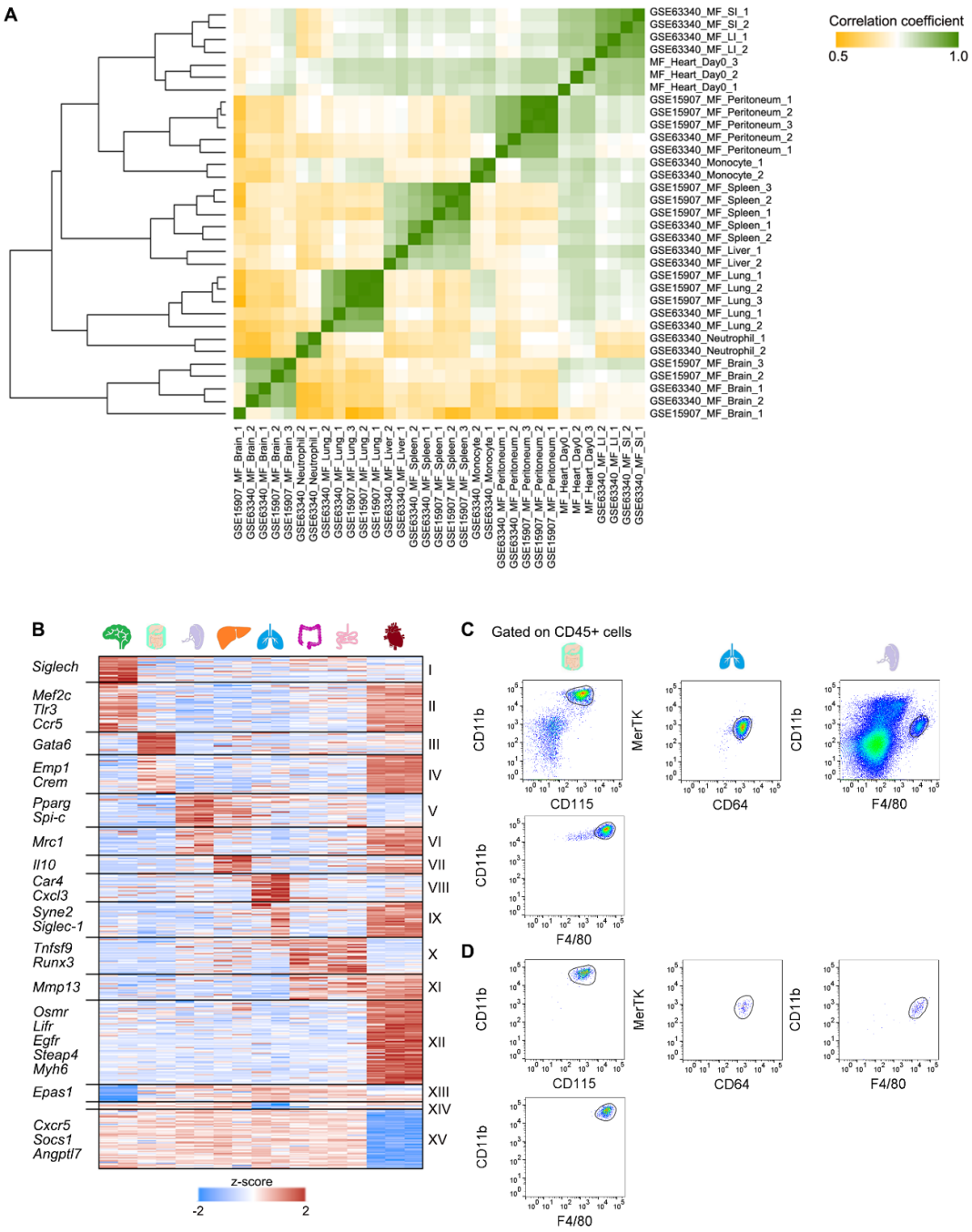

Figure S3. Comparison of tissue-resident Mφs shows a cardiac-macrophage specific gene signature. Related to Figure 1. (A) Pairwise spearman correlation of transcriptional profiles between various tissue-resident Mφs, monocytes, and neutrophils. Labels indicate origin of data (GSE15907, GSE63340, and current study), cell type, and tissue of origin. (B) K-means clustering (k = 15) of genes differentially expressed in at least one tissue comparison. (C) Flow cytometry sorting strategy for tissue-resident Mφs from peritoneum, lung, and spleen. Within the $CD45^+$ cells, peritoneal Mφs are defined as $CD115^+$ $CD11b^+$ $F4/80^+$ cells, lung Mφs as $CD64^+$ $MerTK^+$ cells, and splenic Mφs as $CD11b^{low}$ $F4/80^{high}$ cells. (D) Post-sort of tissue-resident Mφs from peritoneum, lung, and spleen. Images are representative of 3 independent experiments.

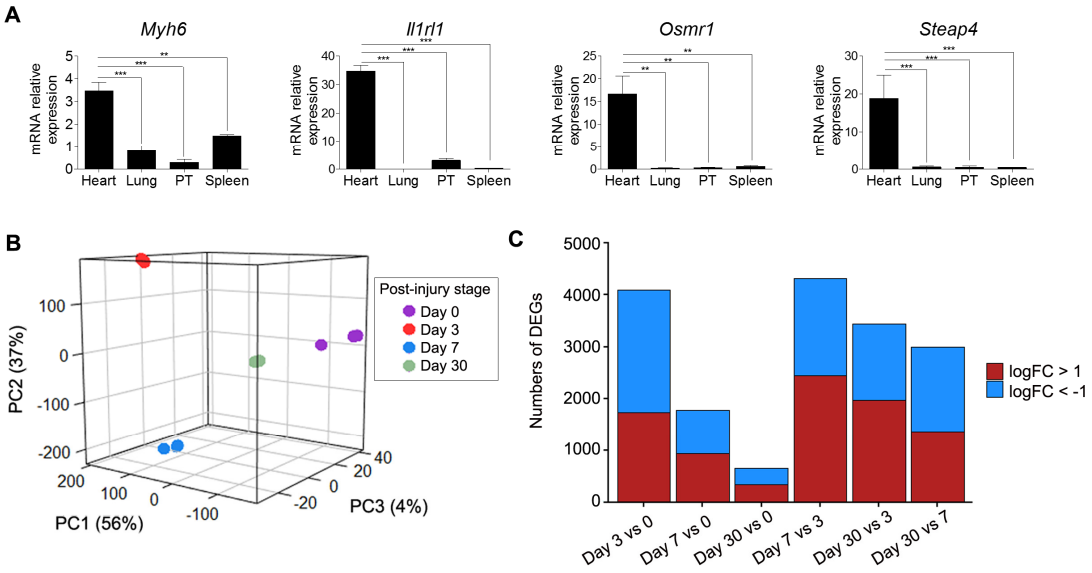

Figure S4. Validation of cardiac-specific markers and global analysis of gene expression changes in cardiac Mφs after injury. Related to Figure 1. (A) mRNA expression levels assessed by qPCR of markers specific for CRMs. Data represent the mean ± SEM of 3 independent experiments; **P<0.01, ***P<0.001 (One way-ANOVA followed by Tukey test). (B) PCA of gene expression in heart Mφs at different post-injury stages. Numbers in parentheses indicate the percentage of variation explained by each of the 3 first principal components. (C) Number of DEG in cardiac Mφs for every comparison across time.

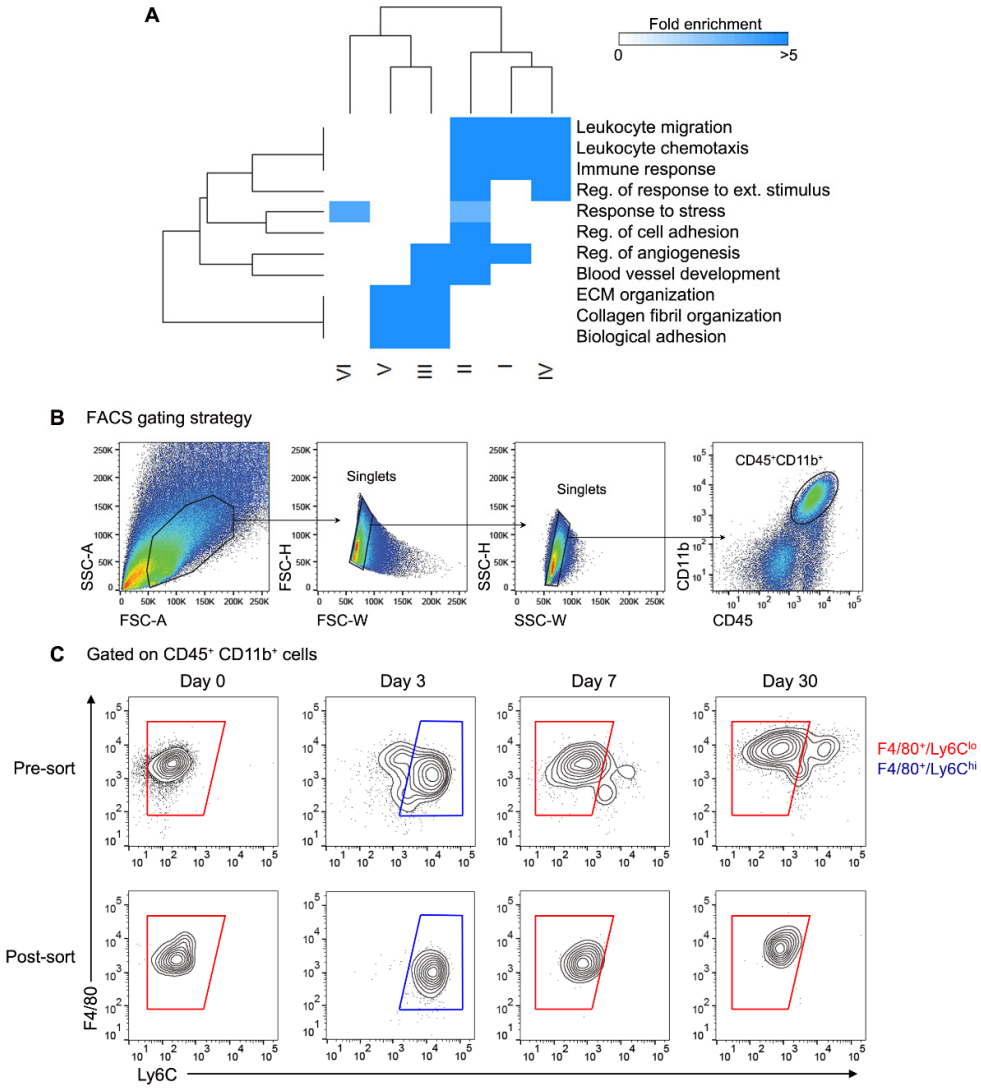

Figure S5. Functional analysis of secretome and characterization of cardiac Mφs in C57BL/6 mice after cryoinjury. Related to Figure 2. (A) Hierarchical clustering of significantly enriched (B-H adj-p < 0.01, Fold-Enrichment > 2) PANTHER biological processes for the secretome. (B) FACS gating strategy for cardiac Mφs at different post-injury stages. (C) Within the $CD45^{+}$ $CD11b^{+}$ cells, the $F4/80^{+}/Ly6C^{low}$ population (red) was sorted at 0, 7, and 30 days post-injury. The $F4/80^{+}/Ly6C^{high}$ population (blue) was purified at 3 days post-injury. Sorting was performed with a pool of 5-10 mice per time point.

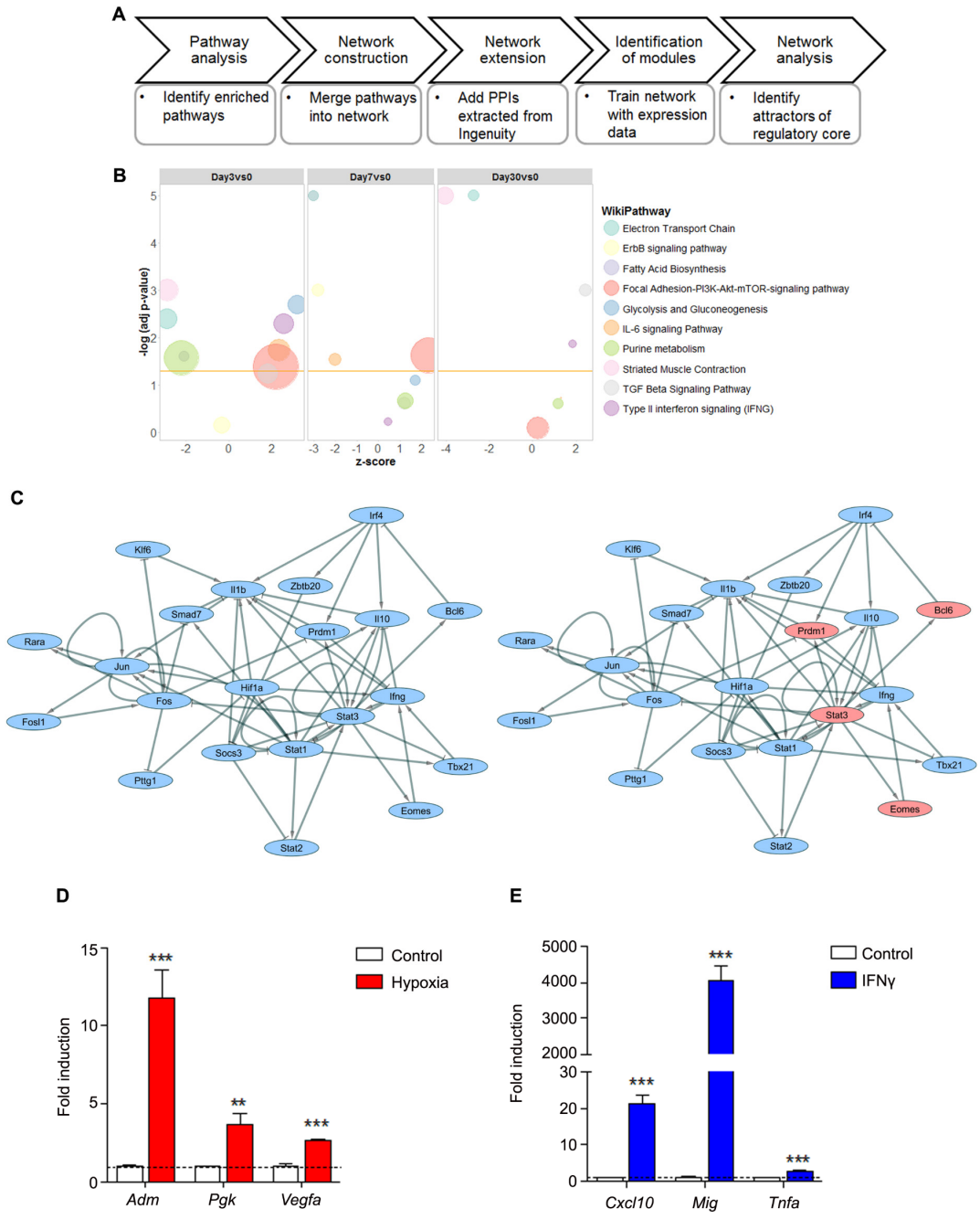

Figure S6. Simulated dynamics identifies a complex regulatory network in post-injury Mφs. Related to Figure 4. (A) *In silico* network analysis workflow. (B) GOBubble of pathways enriched in at least one of the displayed contrasts. X-axis displays z-score of selected pathways. Y-axis corresponds to negative logarithm of the adjusted p-value. Each circle represents one pathway (legend) and the circle size correlates with number of assigned genes to pathway. (C) Point attractors of network stable state analysis. Blue nodes are "off", red nodes are "on". (D) mRNA expression levels of selected hypoxia and (E) IFNγ target genes in *in vitro* peritoneal Mφs, and normalized to control (normoxia without IFNγ treatment). Data represent the mean ± SEM of 3 independent experiments; **P<0.01, ***P<0.001 (unpaired student's t-test).

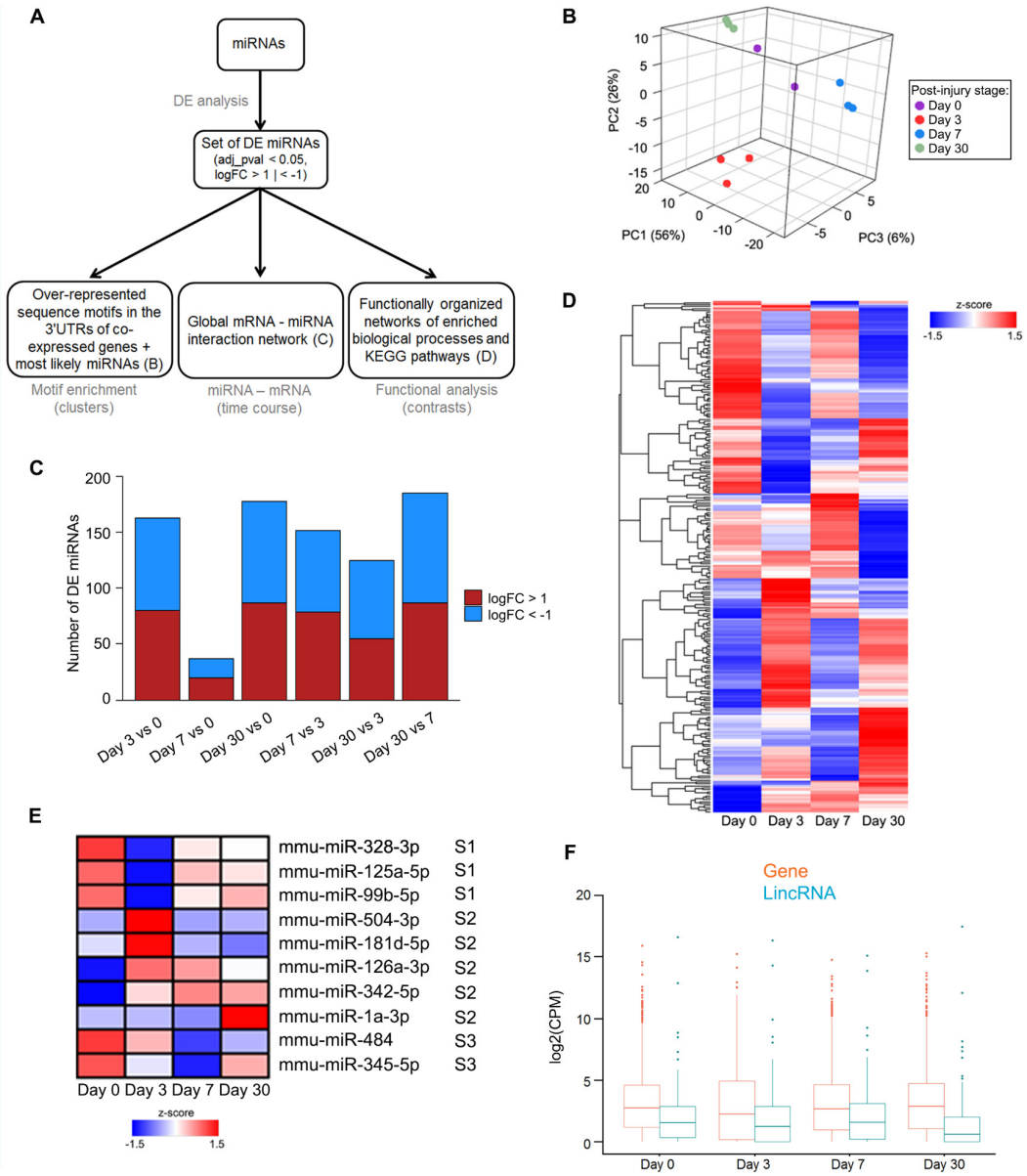

Figure S7. miRNA and lincRNA expression profile of cardiac Mφs. Related to Figures 5 and 7. (A) Workflow of miRNA analysis. (B) PCA of miRNA expression. Number in parenthesis indicate the percentage of variation explained by each of the 3 first principle components. (C) Number of DE miRNAs for every comparison across time. (D) Hierarchical clustering of the 255 miRNAs differentially expressed in at least one time point compared to control. (E) Dendrogram of miRNAs selected from the subnetworks S1, S2, and S3. (F) Box plot of distribution of transcript counts (log_2 CPM) for protein-coding mRNAs vs lncRNAs.

Supplemental Experimental Procedures

Mouse model of myocardial injury

Cryoinjury was performed as previously described (Paik et al., 2015; van Amerongen et al., 2008). Briefly, mice were anesthetized with sevoflurane (4%), and intubated using a 24-gauge intravenous catheter with a blunt end. Mice were artificially ventilated with a mixture of O_2 and air [1:1 (vol/vol)] using rodent ventilator (minivent 845) with 160 strokes/min in a total volume of 250 µl. Mice were placed on heating pad to maintain body temperature at 37°C. A thoracotomy was performed through the fourth left intercostal space, the pericardium was opened, and the heart was exposed. Cryoinjury was induced applying a 3 mm diameter cryoprobe, cooled to -196°C with liquid nitrogen to the anterior left ventricle free wall for 10 seconds. After this, the procedure was repeated twice. The exact position of the probe was carefully set using the left atrium and pulmonary artery as anatomic landmarks. Animals were sacrificed by CO_2 inhalation 3, 7 and 30 days post-injury.

Cell culture

Peritoneal thioglycollate-elicited Mφs were isolated from the peritoneal cavity 3 days after thioglycollate injection. Cells were plated in RPMI supplemented with 10% heat-inactivated FBS and 1%P/S. Cells cultured in normoxia (21% O_2, 5% CO_2) or hypoxia (0.5% O_2, 5% CO_2) were incubated for 24h in the presence or absence of 10ng/mL IFNγ (ThermoFisher).

Flow cytometry and cell sorting

Single-cell suspensions were obtained from heart, spleen, lung and peritoneum. Mice were euthanized by CO_2 inhalation and immediately perfused by intracardiac injection of ice-cold PBS. Right and left atria were removed and the ventricles were minced with fine scissors, and digested in collagenase IV 0.1% (528 U/mg Sigma) in PBS at 37°C for 45 min under gentle shaking. Whole spleen was collected and mechanically disrupted. Peritoneal cells were harvested by peritoneal cavity lavage (10mL of cold PBS). Alveolar cell suspension was obtained by bronchoalveolar lavage (6 times) with 1ml of FACS PBS containing 10% FBS and 5mM EDTA buffer using a blunt syringe (NeBD Biosciences). All samples were filtered through nylon mesh of 100 µm (BD biosciences) to obtain a homogeneous cell suspension, and heart and spleen suspensions were subjected to red blood cells lysis with 1x RBC Lysis buffer solution (eBioscience). The resulting single-cell suspensions were Fc-blocked using anti-mouse CD16/CD32 antibody (BD Pharmingen) 30min at 4ºC in FACS buffer. Antibodies were incubated for 30min at 4ºC in FACS buffer. Where appropriate, cells where further incubated with streptavidin conjugates for 30min at 4ºC. For CD68 and LIFR staining, cells were fixed and permeabilized using a commercial kit (Fixation & Permeabilization, eBioscience). Flow cytometry studies were performed on a BD FACSCanto™ II and subsequently analyzed with FlowJo Software (Tree Star). Cell sorting was performed using BD FACS-ARIA™ II cell sorter (BD Biosciences) and all the samples were sorted into PBS supplemented with 10% FBS. Within the $CD45^+$ cells, peritoneal Mφs are defined as $CD115^+$ $CD11b^+$ $F4/80^+$ cells, lung Mφs as $CD64^+$ $MerTK^+$ cells, and splenic Mφs as $CD11b^{low}$ $F4/80^{high}$ cells. In $CX_3CR1^{GFP/+}$ mouse, within the $CD45^+$ $CD11b^+$ cells, the $Ly6C^{low}/CX_3CR1^{high}$ cardiac Mφs were sorted for 0, 7, and 30 days post-injury, whereas $Ly6C^{high}/CX_3CR1^{low}$ cardiac Mφs were purified for 3 days post-injury. In C57BL/6 mouse, within the $CD45^+$ $CD11b^+$ cells, the $F4/80^+Ly6C^{low}$ cardiac Mφs were sorted for 0, 7, and 30 days post-injury, whereas $F4/80^+Ly6C^{high}$ cardiac Mφs were purified for 3 days post-injury.

The standardized median fluorescence intensity (MFI) was calculated as follows:

$$\text{Standardized MFI} = \frac{(\text{median}_{\text{positive}} - \text{median}_{\text{background}})}{2*\text{SD}_{\text{background}}}$$

Whereas $median_{positive}$ is the median intensity of the positive cell population, $median_{background}$ is the median intensity of the control, and $SD_{background}$ is the standard deviation of the intensity of the control (Maecker et al., 2004). We used Fluorescence Minus One (FMO) Control or Isotype control.

List of used antibodies

Antibody	Provider	Reference
CD45-eFluor450 Rat Anti-Mouse	eBioscience	48-0451
CD45-PerCP-Cy5.5 Rat Anti-Mouse	BD Biosciences	550994
CD11b-Alexa Fluor 647 Rat Anti-Mouse	BD Biosciences	557686
CD11b-PE-Cy7 Rat Anti-Mouse	BD Biosciences	552850
Ly6C-FITC Rat Anti-Mouse	BD Biosciences	553104
Ly6C-APC Rat Anti-Mouse	BD Biosciences	560595
CD40-APC Rat anti-Mouse	BD Biosciences	558695
Lyve1-Biotin Rat Anti-Mouse	eBioscience	13-0443
CD115-PE Rat Anti-Mouse	BioRad	MCA1898PET
CD274-Biotin Rat Anti-Mouse	BioRad	MCA497PE
F4/80-PE Rat Anti-Mouse	Biolegend	124305
F4/80-PE-Cy7 Rat Anti-Mouse	BioLegend	123114
CD64-PE Mouse anti-Mouse	BD Biosciences	558455
CD64-Alexa Fluor 647 Mouse anti-Mouse	BD Biosciences	558539
CD206-Alexa Fluor 647 Rat Anti-Mouse	BioRad	MCA2235A647T
CD68-PerCP-Cy5.5 Rat Anti-Mouse	BioLegend	137010
CD86-PE Rat Anti-Mouse	BD Biosciences	561963
LIF R alpha-PE Rat Anti-mouse	R&D Systems	FAB5990P
EGFR-FITC Rat Anti-mouse/human	Genetex	GTX11400
CD36 Mouse Anti-mouse/rat	Cascade Bioscience	ABM-5525
Isotype Control PE Rat IgG2a	BD Biosciences	557229
Isotype Control Alexa Fluor 647 Rat IgG2a	BioRad	MCA1212A647
Streptavidin-PB conjugate	ThermoFisher Scientific	S11222
Streptavidin-Alexa Fluor 488 conjugate	ThermoFisher Scientific	S11223

Immunofluorescence and confocal microscopy

For immunofluorescence analysis, hearts were fixed in 4% PFA at 4ºC overnight, and subsequently dehydrated in 40% of sucrose. Then, they were embedded and frozen in OCT and sectioned (30µm) with a LeicaCM3050 cryostat. OCT-embedded sections were permeabilized with 0.3% Triton X-100 (Sigma)/ PBS solution, and blocked in 1% goat-serum/ 0.1% Triton X-100/PBS for 1h. Cells were first labeled with primary antibodies (4ºC, overnight) and after with fluorescently labeled secondary antibodies (4ºC, overnight). Nuclei were counterstained with DAPI. Sections were thoroughly washed with PBS before mounting them using FluoroMount-G (SouthernBiotech). Z-stacks of images were processed with Nikon A1R software and 3D-reconstructed with Imaris (version 7.00, Bitplane) software.

List of used antibodies

Antibody	Provider	Reference
Chicken anti-GFP	Abcam	ab13970
Alexa Fluor® 488 Goat Anti-Chicken IgY	Abcam	ab150169
CD68 Rat Anti-Mouse	AbDserotec	MCA1957
Cy™3 Goat Anti-Rat IgG	Jackson ImmunoResearch	112-166-072

RNA isolation and quantitative real-time PCR (q-PCR)

Sorted cells were placed in Tri Reagent (Ambion) for RNA isolation. Total RNA was isolated from 3 independent biological replicates, and RNA quality and quantity measured using the NanoDrop ND100 (Thermo Scientific). Total RNA was reverse-transcribed to cDNA using the High Capacity cDNA Reverse Transcription Kit (Applied Biosystems). qPCR analysis was performed using Sybr Green probes in the AB7900 FAST 384 Detection System (Applied Biosystems), according to the

manufacturer´s instructions. Gene expression values were normalized to the housekeeping genes *36b4* and *Cyclophilin*, and expressed as relative mRNA level. Data were analyzed by qBASE program (Biogazelle) obtaining the Ct of the amplification products.

Primers for q-PCR

Gene	**Sequence**
Mrc1	F-ATTGTGGAGCAGATGGAAGG R-TGAATGGAAATGCACAGACG
Cd40	F-GTGTCTTTGCCTCGGCTGT R- GCCATCGTGGAGGTACTGTT
Cd86	F-GGGCTTGGCAATCCTTATCT R-CCAGCTCACTCAGGCTTATG
Stat3	F-TCTGTCAGATGCCAAATGCT R-CTTGGTGGTGGACGAGAACT
Il10	F-TGAATTCCCTGGGTGAGAAG R-TCACTCTTCACCTGCTCCACT
Stat1	F-TGCATAGAGCAGGAAATCAAGA R-CCTGTTTTTGGTCGCTCTTC
Hif1a	F-GAATGCTCAGAGGAAGCGAAA R-ACAGTCACCTGGTTGCTGCA
Cd274	F-GCTTCTCAATGTGACCAGCA R-CTGTGGAGGATGTGTTGCAG
Egfr	F-ACACTGCTGGTGTTGCTGAC R-CCTCTGCAGGCTCAGAAAGT
Lifr	F-CGGCCAAGAAATCCATAACT R-AACGAAGTCGGATCATGAGG
Lyve1	F-AGAATGGCAAAGGTGTCCTG R-GTCCAACACGGGGTAAAATG
Osmr	F-GAATGGAAGACGCATTGTGA R-CTGGTGCCCAGACACAGTAG
Jun	F-TCCCCTATCGACATGGAGTC R-TTTTGCGCTTTCAAGGTTTT
Cd36	F-CCAAGCTATTGCGACATGA R-AGATCCGAACACAGCGTAGA
Steap4	F-TTCGATGGAGGCTGAGAAAT R-CAGCGCCAAGTAGGAATCAT
Il1rl1	F-GCGGAGAATGGAACCAACTA R-TCCATTGTGTGGTTGTATGGA
Myh6	F-TGGTCACCAACAACCCATACGACT R-TGTCAGCTTGTAGACACCAGCCTT
Adm	F-AGCATCCAGCAGCTACCCTA R-GGTAGCGTTTGACACGAATG
Pgk1	F-TTCCAACAAGCTGACTTTGG R-TTTGGTTGTTTGTTATCTGGTTG
Vegfa	F-GCGAGGCAGCTTGAGTTAAA R-TCTTTCCGGTGAGAGGTCTG
Cxcl10	F-TCCCTGCGAGCCTATCCTG R-TTTTCATCGTGGCAATGATCTC
Mig	F-GATAAGGAATGCACGATGCTC R-TCTCCGTTCTTCAGTGTAGCAA
Tnfa	F-CCAGACCCTCACACTCAGATC R-CACTTGGTGGTTTGCTACGAC
36b4	F-GCGACCTGGAAGTCCAACTA R-ATCTGCTGCATCTGCTTGG

Cyclo	F-ACAGGTCCTGGCATCTTGTC R-CATGGCTTCCACAATGTTCA

mRNA profile analysis

Fastq files containing raw reads for each library were extracted from the GAIIx sequencer and de-multiplexed using the CASAVA pipeline (Illumina). Sequencing adaptor contaminations were removed from reads using cutadapt software (version 1.3) (Martin, 2011) and the resulting reads were mapped and quantified on the transcriptome (GRCm38) using RSEM (version 1.2.20) (Li and Dewey, 2011). Trimmed mean of M-values (TMM) normalization method was applied to estimated counts from RSEM. The resulting $\log_2$ CPMs were used as a proxy of gene expression in each sample. Genes were kept if they were expressed (> 1CPM) in at least 6 samples. PCA was applied to the $\log_2$ CPMs of filtered genes and all samples ('rgl' R package version 0.98.1, https://CRAN.R-project.org/package=rgl). Gene expression differences were assessed using the edgeR package (Robinson et al., 2010) with false discovery rate (FDR) correction for multiple testing. Genes with FDR < 0.05 and an absolute logFC > 1 were considered differentially expressed (DE). The R package clValid was used to determine the optimal number of clusters for k-means clustering based on internal measures (Brock et al., 2011). K-means clustering was performed on $\log_2$ CPMs of genes DE in at least one condition using GENESIS software. A heatmap of normalized expression values for each cluster was created using the ggplot2 package (Wickham and Chang, 2009). To identify overrepresented biological categories PANTHER classification system version 11.1, based on the Gene Ontology (GO) database (version 1.2, annotations 2017-04-24), was applied with default settings using the annotation dataset 'GO biological process complete'. Bonferroni correction was used to correct for multiple testing. Terms with a fold- enrichment > 2 and an adjusted p-value < 0.01 were further considered.

Tissue resident transcriptional signature analysis

Gene expression data series were downloaded from the NCBI Gene Expression Omnibus (GEO) for tissue Mφs (GSE15907, GSE63340) (Gautier et al., 2012; Lavin et al., 2014). Data were normalized, log transformed and adjusted for batch effects using the comBat function implemented in the R package sva (Leek et al., 2012). A correlation matrix was calculated and visualized with the heatmap.2 function of the R package gplots (gplots version 3.0.1., https://CRAN.R-project.org/package=gplots). DE analysis was carried out with the edgeR package and genes DE in at least one of the contrasts (adjusted p-value < 0.05) were further grouped by k-means clustering. A heatmap of normalized expression values for each cluster was created using the ggplot2 package.

Secretome and receptome analysis

We curated semiautomatically a list of secretome (molecules secreted) and receptome components (membrane proteins with an extracellular portion that interacts with molecules of the local environment). Gene lists were filtered regarding their annotation to one of the following terms from the GO_CC hierarchy: "extracellular region" (GO:0005576), "extracellular space" (GO:0005615), "cell surface" (GO:0009986) and "extracellular matrix" (GO:0031012). Subsequently, predicted and validated information from the Human Protein Atlas (Uhlen et al., 2015) was used to classify cellular location of the proteins encoded by our list the selected genes more precisely. The frequency of secretome and receptome molecules was calculated per cluster. For display, secretome and receptome components were selected for the clusters I, II, III and VI based on logFC and adjusted p-value. Only secretome and receptome molecules with a logFC > 1 in all relevant contrasts were kept, ranked by increasing adjusted p-value and a maximum of 10 molecules per temporal stage were selected. The cellular localization of the encoded proteins was confirmed in the literature. The PANTHER classification system was used to perform the functional analysis of secretome and receptome. The STRING database was used to get known and predicted interactions for all secretome and receptome. The active prediction methods "co-expression", "experiments", "databases" and "text mining" and a score > 0.8 were selected. Subsequently, the list of possible interactions for the secretome was crossed with the list of predicted receptome-ligand pairs to distinguish *in silico* between heterotypic and homotypic paracrine signaling.

Transcription factors

The iRegulon App (Janky et al., 2014) was applied to each cluster to search for enriched motifs 20kb centered around the TSS of the co-expressed genes and to link enriched motifs to known TF binding sites. The resulting list of enriched motifs was filtered and only motifs that are potentially recognized by at least one DE TF were kept. Enriched motifs were ranked by decreasing normalized enrichment score (NES) applying the default iRegulon NES cutoff of 3.0. The GOCluster function of the R package GOplot (Walter et al., 2015) was used to visualize hierarchical clustering and expression profiles of DE nuclear receptors (adjusted p-value < 0.05).

miRNA profile analysis

Intensity data from microarray images were extracted with Feature Extraction Software (Agilent Technologies). The total gene signal was quantile normalized and miRNAs were kept if they were expressed (flag present) in at least 6 samples. PCA was applied to the whole miRNA expression profile of all samples. LIMMA (Smyth, 2005) was used to analyse differential expression of miRNAs with correction for multiple comparisons. miRNAs with a FDR < 0.05, an absolute logFC > 1 and a mean expression value > 2.0 were considered differentially expressed (DE). DE miRNAs were clustered with the average linkage method.

miRNA-mRNA interactions

Motif enrichment miRvestigator (Plaisier et al., 2011) was used to search for enriched motifs within the 3'UTR of co-expressed genes and to identify the most likely miRNAs regulating these genes. The parameters used were default settings except: seed models = 6mer, 7mer and model wobble base-pairing = 'yes'. The resulting list was filtered and only miRNAs anti-correlated to the median expression profile of the target cluster were kept.

Global miRNA-mRNA interaction network

DE miRNAs were used as input for mirWalk (Dweep et al., 2014) to predict mRNA targets based on the mirWalk and TargetScan algorithm. Only DE targets were kept and the remaining list of interactions was filtered based on expression (anti-correlation, correlation coefficient (CC) < -0.9). Cytoscape (Shannon et al., 2003) was used to visualize the resulting list of 31196 mRNA-miRNA interactions. The perfuse force directed layout was applied to improve comprehensibility. Node color was mapped to the normalized expression values at various temporal stages.

Functional analysis of miRNAs

To identify the role of miRNAs in Mφ transition, miRNAs DE in the contrast day 7 vs day 3 were used as input for mirWalk to predict mRNA targets. The interactions were filtered as described before and they were automatically split into 2 networks according to miRNA expression (miRNA upregulation at days 3 or 7). Functional analysis of the networks was performed with the cytoscape plugin ClueGO. GO Biological process and KEGG Pathway with evidence on the level 'All_experimental' were selected as ontologies/pathways. The 'GO Term Fusion' option was applied to reduce term redundancy and only terms with an adjusted p-value < 0.05 (Bonferroni step down) were displayed. GO Term grouping was applied with fixed group coloring. Initial group size was set to 2 and a 35% overlap was set as threshold to merge groups. For each group the most significant term was displayed.

lincRNA analysis

Ensembl biotype information (Aken et al., 2016) was used to classify DEGs as lincRNAs. Based on the ceRNA hypothesis (Salmena et al., 2011) 3'UTR sequences were blasted against lincRNA sequences to search for sequence similarities. The aligned sequences were scanned for common miRNA seed sequences (7mer, perfect match, starting at 1st position). Possible mRNA-lincRNA-miRNA triangles were further filtered by expression and only interactions with CC > 0.7 or CC < -0.7 were kept. The BEDOPS closest-features program with the no-overlap option was used to identify the closest protein-coding genes upstream and downstream of each lincRNA (Neph et al., 2012). The reported list was filtered to exclude protein coding genes that were not DE. Cytoscape was used to create small networks

where 2 protein coding genes were connected through at least one lincRNA. ClueGO (Bindea et al., 2009) was used to analyze the function of associated genes with the same settings as described above. The R package HiveR (HiveR Version 0.2.55, academic.depauw.edu/~hanson/HiveR/HiveR.html) was used to create the hive plot.

Supplemental References

Aken, B.L., Ayling, S., Barrell, D., Clarke, L., Curwen, V., Fairley, S., Fernandez Banet, J., Billis, K., García Girón, C., Hourlier, T.*, et al.* (2016). The Ensembl gene annotation system. Database *2016*, 1-19.

Bindea, G., Mlecnik, B., Hackl, H., Charoentong, P., Tosolini, M., Kirilovsky, A., Fridman, W.-H., Pagès, F., Trajanoski, Z., and Galon, J. (2009). ClueGO: a Cytoscape plug-in to decipher functionally grouped gene ontology and pathway annotation networks. Bioinformatics *25*, 1091-1093.

Brock, G., Pihur, V., Datta, S., and Datta, S. (2011). clValid, an R package for cluster validation. J Stat Softw.

Dweep, H., Gretz, N., and Sticht, C. (2014). miRWalk database for miRNA-target interactions. Methods Mol. Biol. *1182*, 289-305.

Garg, A., Mohanram, K., Di Cara, A., De Micheli, G., and Xenarios, I. (2009). Modeling stochasticity and robustness in gene regulatory networks. Bioinformatics *25*, i101-109.

Gaujoux, R., and Seoighe, C. (2013). CellMix: a comprehensive toolbox for gene expression deconvolution. Bioinformatics *29*, 2211-2212.

Gautier, E.L., Shay, T., Miller, J., Greter, M., Jakubzick, C., Ivanov, S., Helft, J., Chow, A., Elpek, K.G., Gordonov, S.*, et al.* (2012). Gene-expression profiles and transcriptional regulatory pathways that underlie the identity and diversity of mouse tissue macrophages. Nat. Immunol. *13*, 1118-1128.

Ideker, T., Ozier, O., Schwikowski, B., and Siegel, A.F. (2002). Discovering regulatory and signalling circuits in molecular interaction networks. Bioinformatics *18*, S233-S240.

Janky, R., Verfaillie, A., Imrichova, H., Van de Sande, B., Standaert, L., Christiaens, V., Hulselmans, G., Herten, K., Naval Sanchez, M., Potier, D.*, et al.* (2014). iRegulon: from a gene list to a gene regulatory network using large motif and track collections. PLoS Comput. Biol. *10*, e1003731.

Kelder, T., van Iersel, M.P., Hanspers, K., Kutmon, M., Conklin, B.R., Evelo, C.T., and Pico, A.R. (2012). WikiPathways: building research communities on biological pathways. Nucleic Acids Res. *40*, D1301-D1307.

Kutmon, M., van Iersel, M.P., Bohler, A., Kelder, T., Nunes, N., Pico, A.R., and Evelo, C.T. (2015). PathVisio 3: an extendable pathway analysis toolbox. PLoS Comput. Biol. *11*, e1004085.

Lavin, Y., Winter, D., Blecher-Gonen, R., David, E., Keren-Shaul, H., Merad, M., Jung, S., and Amit, I. (2014). Tissue-resident macrophage enhancer landscapes are shaped by the local microenvironment. Cell *159*, 1312-1326.

Leek, J.T., Johnson, W.E., Parker, H.S., Jaffe, A.E., and Storey, J.D. (2012). The sva package for removing batch effects and other unwanted variation in high-throughput experiments. Bioinformatics *28*, 882-883.

Li, B., and Dewey, C.N. (2011). RSEM: accurate transcript quantification from RNA-Seq data with or without a reference genome. BMC Bioinformatics *12*, 1-16.

Li, L., Ng, D.S., Mah, W.C., Almeida, F.F., Rahmat, S.A., Rao, V.K., Leow, S.C., Laudisi, F., Peh, M.T., Goh, A.M.*, et al.* (2015). A unique role for p53 in the regulation of M2 macrophage polarization. Cell Death Differ. *22*, 1081-1093.

Maecker, H.T., Frey, T., Nomura, L.E., and Trotter, J. (2004). Selecting fluorochrome conjugates for maximum sensitivity. Cytometry Part A *62*, 169-173.

Martin, M. (2011). Cutadapt removes adapter sequences from high-throughput sequencing reads. EMBnet.journal *17*, 10-12.

Neph, S., Kuehn, M.S., Reynolds, A.P., Haugen, E., Thurman, R.E., Johnson, A.K., Rynes, E., Maurano, M.T., Vierstra, J., Thomas, S.*, et al.* (2012). BEDOPS: high-performance genomic feature operations. Bioinformatics *28*, 1919-1920.

Paik, D.T., Rai, M., Ryzhov, S., Sanders, L.N., Aisagbonhi, O., Funke, M.J., Feoktistov, I., and Hatzopoulos, A.K. (2015). Wnt10b Gain-of-Function Improves Cardiac Repair by Arteriole Formation and Attenuation of Fibrosis. Circ. Res. *117*, 804-816.

Plaisier, C.L., Bare, J.C., and Baliga, N.S. (2011). miRvestigator: web application to identify miRNAs responsible for co-regulated gene expression patterns discovered through transcriptome profiling. Nucleic Acids Res. *39*, W125-W131.

Robinson, M.D., McCarthy, D.J., and Smyth, G.K. (2010). edgeR: a Bioconductor package for differential expression analysis of digital gene expression data. Bioinformatics *26*, 139-140.

Rodriguez, A., Crespo, I., Androsova, G., and del Sol, A. (2015). Discrete Logic Modelling Optimization to Contextualize Prior Knowledge Networks Using PRUNET. PLoS ONE *10*, e0127216.

Salmena, L., Poliseno, L., Tay, Y., Kats, L., and Pandolfi, P.P. (2011). A ceRNA hypothesis: the Rosetta Stone of a hidden RNA language? Cell *146*, 353-358.

Shannon, P., Markiel, A., Ozier, O., Baliga, N.S., Wang, J.T., Ramage, D., Amin, N., Schwikowski, B., and Ideker, T. (2003). Cytoscape: a software environment for integrated models of biomolecular interaction networks. Genome Res. *13*, 2498-2504.

Smyth, G.K. (2005). Limma: linear models for microarray data. In Bioinformatics and computational biology solutions using R and Bioconductor (Springer), pp. 397-420.

Uhlen, M., Fagerberg, L., Hallstrom, B.M., Lindskog, C., Oksvold, P., Mardinoglu, A., Sivertsson, A., Kampf, C., Sjostedt, E., Asplund, A.*, et al.* (2015). Proteomics. Tissue-based map of the human proteome. Science *347*, 1260419.

van Amerongen, M.J., Harmsen, M.C., Petersen, A.H., Popa, E.R., and van Luyn, M.J. (2008). Cryoinjury: a model of myocardial regeneration. Cardiovascular pathology : the official journal of the Society for Cardiovascular Pathology *17*, 23-31.

Walter, W., Sanchez-Cabo, F., and Ricote, M. (2015). GOplot: an R package for visually combining expression data with functional analysis. Bioinformatics *31*, 2912-2914.

Wickham, H., and Chang, W. (2009). ggplot2: An implementation of the Grammar of Graphics. In R package.

Zinovyev, A., Viara, E., Calzone, L., and Barillot, E. (2008). BiNoM: a Cytoscape plugin for manipulating and analyzing biological networks. Bioinformatics *24*, 876-877.